SANDIA REPORT
SAND2012-9770
Unlimited Release
Printed November, 2012

2169 Steel Waveform Experiments

Michael D. Furnish[1], C. Scott Alexander[1], William D. Reinhart[2] and Justin L. Brown[1]

[1]Dynamical Material Properties Department 1646
[2]Solid Dynamics Experiments Department 1647

Prepared by
Sandia National Laboratories
Albuquerque, New Mexico 87185 and Livermore, California 94550

Sandia National Laboratories is a multi-program laboratory managed and operated by Sandia Corporation, a wholly owned subsidiary of Lockheed Martin Corporation, for the U.S. Department of Energy's National Nuclear Security Administration under contract DE-AC04-94AL85000.

Approved for public release; further dissemination unlimited.

Sandia National Laboratories

Issued by Sandia National Laboratories, operated for the United States Department of Energy by Sandia Corporation.

NOTICE: This report was prepared as an account of work sponsored by an agency of the United States Government. Neither the United States Government, nor any agency thereof, nor any of their employees, nor any of their contractors, subcontractors, or their employees, make any warranty, express or implied, or assume any legal liability or responsibility for the accuracy, completeness, or usefulness of any information, apparatus, product, or process disclosed, or represent that its use would not infringe privately owned rights. Reference herein to any specific commercial product, process, or service by trade name, trademark, manufacturer, or otherwise, does not necessarily constitute or imply its endorsement, recommendation, or favoring by the United States Government, any agency thereof, or any of their contractors or subcontractors. The views and opinions expressed herein do not necessarily state or reflect those of the United States Government, any agency thereof, or any of their contractors.

Printed in the United States of America. This report has been reproduced directly from the best available copy.

Available to DOE and DOE contractors from
U.S. Department of Energy
Office of Scientific and Technical Information
P.O. Box 62
Oak Ridge, TN 37831

Telephone: (865) 576-8401
Facsimile: (865) 576-5728
E-Mail: reports@adonis.osti.gov
Online ordering: http://www.osti.gov/bridge

Available to the public from
U.S. Department of Commerce
National Technical Information Service
5285 Port Royal Rd.
Springfield, VA 22161

Telephone: (800) 553-6847
Facsimile: (703) 605-6900
E-Mail: orders@ntis.fedworld.gov
Online order: http://www.ntis.gov/help/ordermethods.asp?loc=7-4-0#online

SAND2012-9770
Unlimited Release
Printed November, 2012

2169 Steel Waveform Experiments

Michael D. Furnish, C. Scott Alexander, William D. Reinhart and Justin L. Brown
Dynamic Material Properties Department
and Solid Dynamics Experiments Department

Sandia National Laboratories
P.O. Box 5800
Albuquerque NM 87185-1195

Abstract

In support of LLNL efforts to develop multiscale models of a variety of materials, we have performed a set of eight gas gun impact experiments on 2169 steel (21% Cr, 6% Ni, 9% Mn, balance predominantly Fe). These experiments provided carefully controlled shock, reshock and release velocimetry data, with initial shock stresses ranging from 10 to 50 GPa (particle velocities from 0.25 to 1.05 km/s). Both windowed and free-surface measurements were included in this experiment set to increase the utility of the data set, as were samples ranging in thickness from 1 to 5 mm. Target physical phenomena included the elastic/plastic transition (Hugoniot elastic limit), the Hugoniot, any phase transition phenomena, and the release path (windowed and free-surface). The Hugoniot was found to be nearly linear, with no indications of the Fe $\alpha - \varepsilon$ phase transition. Releases were non-hysteretic, and relatively consistent between 3- and 5-mm–thick samples (the 3 mm samples giving slightly lower wavespeeds on release). Reshock tests with explosively welded impactors produced clean results; those with glue bonds showed transient releases prior to the arrival of the reshock, reducing their usefulness for deriving strength information. The free-surface samples, which were steps on a single piece of steel, showed lower wavespeeds for thin (1 mm) samples than for thicker (2 or 4 mm) samples. A configuration used for the last three shots allows release information to be determined from these free surface samples. The sample strength appears to increase with stress from ~1 GPa to ~ 3 GPa over this range, consistent with other recent work but about 40% above the Steinberg model.

Acknowledgments

We gratefully acknowledge the assistance of Tom Thornhill in fielding these shots at the Sandia STAR Facility, and of Heidi Anderson in building up the experiment hardware. Tom Thornhill and Keith Hodge set up the 19-beam VISAR system required for the optical timing method used in those same three shots. This work was done in collaboration with Lawrence Livermore National Laboratory, and we gratefully acknowledge Mukul Kumar, Bryan Reed, and Jeff Florando of LLNL for helpful discussions. Sandia National Laboratories is a multi-program laboratory managed and operated by Sandia Corporation, a wholly owned subsidiary of Lockheed Martin Corporation, for the U.S. Department of Energy's National Nuclear Security Administration under Contract DE-AC04-94AL85000.

Table of Contents

1.0 Introduction and Background 7
2.0 Impact Experiments – Method 8
  2.1 Notional Description 8
  2.2 Detailed specifications 10
3.0 Impact Experiments - Results 12
  3.1 Hugoniot and Loading Wave Structures 12
  3.2 Free surface waveforms 14
  3.3 Waveforms for windowed samples 15
4.0 Impact experiments: Hugoniot state strength interpretation 17
  4.1 General discussion of strength in these experiments 17
  4.2 Impedance matching interpretation 20
  4.3 Transfer function interpretation 23
5.0 Summary 29
References 30
Appendix A: Further discussion of target geometries 32
Appendix B: Data and Lagrangian reduction plots and tables not presented earlier 36
Distribution 41

Figures

1.1 Metallography of pretest sample 7
2.1 Standard shot configuration 8
2.2 Cross-section of explosively-bonded interface between 2169 steel and tantalum 9
2.3 Standard shot configuration (shots 6 – 8) 10
2.3 View of target plate from projectile 11
3.1 Hugoniot results for 2169 steel 13
3.2 Scaled loading portions of waveforms for SS-6 and SS-7 14
3.3 Scaled free surface waveforms for SS 6 – 8. 15
3.4 Windowed sample waveforms for SS 6 - 8 16
3.5 Shot SS-1 release and reshock waveforms (windowed samples) 16
3.6 Velocity histories from windowed samples in shots SS1 – SS5 subjected to compression/release cycle 17
4.1 Position/time diagram of wave interactions for windowed release wave experiments and associated idealized velocity history measured by VISAR 18
4.2 Schematic for determining resolved shear stress from velocity profiles for paired release and reshock experiments 19
4.3 Stress-strain representation of loading / release paths for the 2169 steel 21
4.4 Wave speed – particle velocity representation of loading / release paths for the 2169 steel 22
4.5 Wave speed – particle velocity representation of release and reloading paths 22

4.6 Integration spaces and values for $\Delta\tau_u$ and $\Delta\tau_r$ for shots SS6, 7, 8 using REDUCE analysis 23
4.7 Flow of information in the transfer function interpretation 24
4.8 Transfer function analysis for SS7 26
4.9 Transfer function results for SS6 – 8 (wavespeed/particle velocity space), juxtaposed on Reduce results 26
4.10 Integration spaces and values for $\Delta\tau_u$ and $\Delta\tau_r$ for shots SS6, 7, 8 (5 mm samples), using transfer function analysis 27
4.11 Yield strength Y = $\Delta\tau_u + \Delta\tau_r$ for SS-6, 7, 8 28
A.1 View of target geometry plate from projectile. 32
A.2 Top view of free surface sample (shots SS1-SS5) 32
A.3 Configuration used in CTH simulations of stepped sample 33
A.4 Results of CTH simulations of free surface sample 33
A.5 Experimental waveform of free surface samples for test SS-3. 34
A.6 Design of stepped sample used in tests SS6 – SS8 34
A.7 Results of CTH calculations for a 900 m/s LiF release experiment 35
A.8 Results of CTH calculations for 900 m/s sapphire window reshock experiment 35
B.1 Velocity histories for free surface (stepped samples) spots on SS-1 through SS-5 36
B.2 Velocity histories for windowed spots on SS1 through SS-5 37
B.3 Integration spaces and values for $\Delta\tau_u$ and $\Delta\tau_r$ for shots SS6, 7, 8 (3 mm samples) 37
B.4 Integration spaces and values for $\Delta\tau_u$ for shots SS1 - 5 (5 mm samples) 29
B.5 Integration spaces and values for $\Delta\tau_u$ for shots SS1 - 5 (3 mm samples) 29

Tables

2.1 Hugoniot conditions for 2169 steel experiments (summary tabulation) 10
2.2 Detailed shot parameters for 2169 steel experiments SS1 – SS5 11
2.3 Detailed shot parameters for 2169 steel experiments SS6 – SS8 11
4.1 Strength values at Hugoniot conditions for tests SS-6 – SS-8 27
B.1 Detailed Hugoniot and precursor conditions – windowed samples 38
B.2 Detailed Hugoniot and precursor conditions – free surface samples 38

2169 Steel Waveform Experiments

1.0 Introduction and Background

We have performed a set of gas gun impact experiments to measure strength properties of 2169 steel (21% Cr, 6% Ni, 9% Mn, balance Fe), partially in support of LLNL efforts to develop multiscale models of a variety of materials [Reed, et al, 2011a,b]. This set of experiments was designed to supply carefully controlled shock, reshock and release velocimetry data for this steel, with initial shock stresses ranging from 10 to 50 GPa. Both windowed and free-surface measurements were included in this experiment set to increase the utility of the data set. Physical phenomena studied included the elastic/plastic transition (Hugoniot elastic limit, or HEL), the Hugoniot, any phase transition phenomena, the release path (windowed and free-surface), and finally the dynamic strength.

Two earlier studies of similar material [Wise and Mikkola, 1988; Huang et al., 1994], both using planar impacts on gas guns, showed 2-wave loading structures consistent with an HEL of ~1.3 GPa (Huang) or 1.8 GPa (Wise). The Huang material had a finer grain size (44 μm) than the Wise material (80 μm) and a somewhat different anneal history (water quench vs. vacuum cool down from ~1050°C). As well, the Huang study used free surfaces, while the Wise study used windows. Both materials showed a Hugoniot devoid of the well-known iron $\alpha - \varepsilon$ transition at 13 GPa and lying intermediate between the two phases in $U_S - U_P$ space (shock velocity plotted as a function of post-shock material velocity). A third study, just published [Whiteman and Millett, 2012] used lateral manganin gages over the stress region 0 - 15 GPa.

The present material, provided by LLNL, was found to have relatively equiaxed grains averaging ~40 μm and density of 7.83 ± 0.02 gm/cm^3. Ultrasonic measurements showed a mean longitudinal sound speed of 5.75 km/s and shear sound speed of 3.15 km/s. The key impurities were (ppm by weight) N (2660), Si (2400), V (1500), Mo (940), Co (615), C (305), Nb (250), and O (1.8). A representative metallographic section is shown in Fig. 1.1.

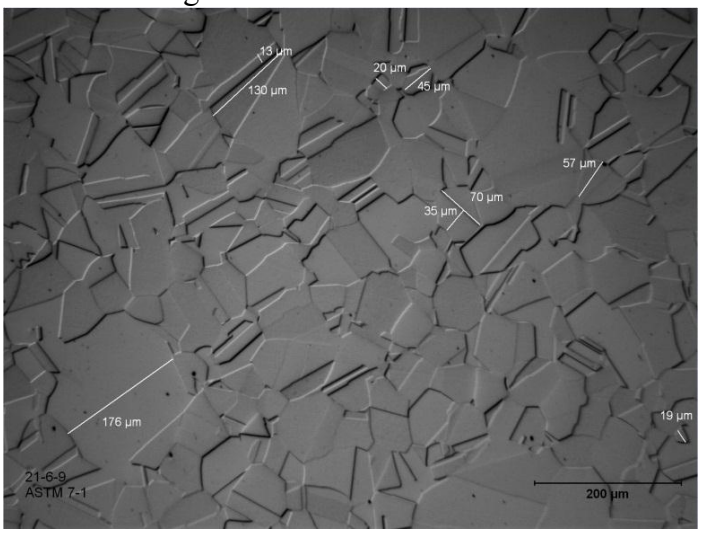

Figure 1.1. Metallography of pretest sample.

2.0 Impact Experiments - Method

2.1 Notional description

In keeping with the objective of measuring a multifaceted set of waveforms under conditions allowing useful comparisons, these shots were designed to accommodate multiple samples on each target. In this way, each shot provided six waveforms, including release and reshock as well as free-surface and windowed measurements. The target configuration for the first five shots is shown in Fig. 2.1; the final three shots used a configuration with modifications as described below. Sapphire was used as the window material for the lowest-stress tests due to its good shock impedance match ($C_0\rho_0$) to the steel ($C_0\rho_0$ is 35.06 for this steel, 44.59 for sapphire and 13.59 for LiF, in units of 10^6 kg/(m^{2}s). Because sapphire yields at ~14 GPa, and loses transparency, lithium fluoride (LiF) windows were used at higher stress levels.

The primary diagnostic was VISAR (Velocity Interferometry System for Any Reflector) [Barker and Hollenbach, 1971], which measures interface velocities via the Doppler shift of laser light reflected from the interface.

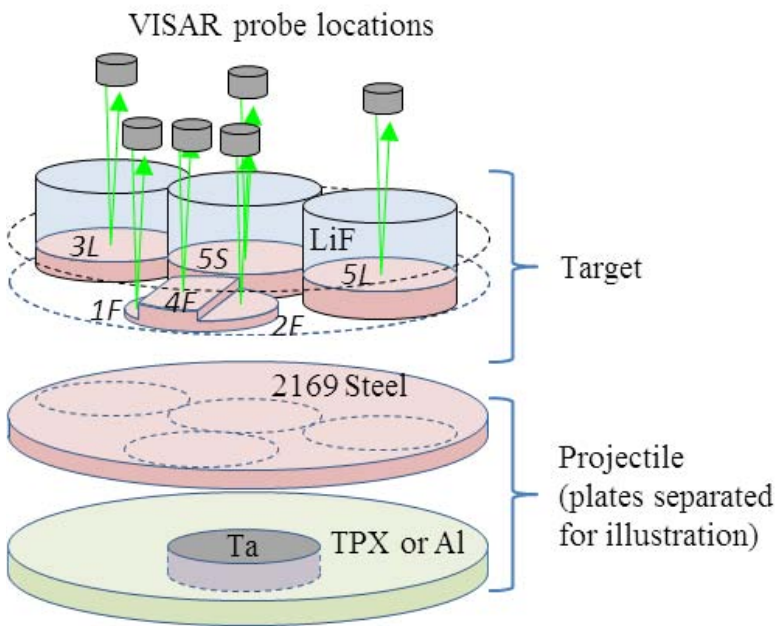

Figure 2.1. Standard shot configuration (shots 1 – 5). Electrical shorting shot pins (velocity and tilt) are not shown. Sample names are 3L = 3 mm shock/release, 5L = 5 mm shock/release, 5R = 5 mm shock/reshock, 1, 2, 4F = 1 2, 4 mm free-surface shock/release. Sample diameters were all 25.4 mm. Release toroid was TPX for shots 1 – 2 and Al for shots 3 – 5. For shot SS-1, the windows were Z-cut sapphire instead of LiF.

In each shot, all but one of the samples experienced an initial loading with the impact of the steel flyer, followed by a release generated at the interface between the flyer and the underlying lower-impedance TPX or aluminum (Fig. 2.1). The center sample experienced the same initial loading, followed by a reshock generated at the interface between the flyer and the underlying higher-impedance tantalum.

A range of sample thicknesses were chosen so that we could determine whether highly rate-sensitive processes were affecting wave propagation.

The configuration was chosen with a combination of free-surface measurements and windowed measurements to allow additional flexibility in model validation. The free surface measurements are valuable because no approximations of window properties (optical or mechanical) are needed. On the other hand, the measurements using LiF and sapphire windows are valuable because (1) the mechanical and optical properties of LiF and sapphire under shock compression have been well documented [Barker and Hollenbach, 1970; Setchell, 1979; Wise and Chhabildas, 1986], and (2) a window is desirable because it reduces the amplitude of the release wave propagating back into the sample from the sample/window interface relative to that from a free surface, resulting in less characteristic bending and therefore less need for iterative methods to determine the sample response to dynamic compression and release[1]. As well, for release experiments a window can prevent spallation.

Although ideally the tilt pins would provide a time base for measuring wave propagation time, in practice these have not been accurate enough (± 5 - 10 ns), so we have assumed that the toe of the elastic wave propagates at the ultrasonically-measured longitudinal sound speed.

A final three shots were conducted with three changes in configuration from the earlier series. First, the projectile impactors were built using a novel process of explosively bonding commercially available 2169 stainless steel and tantalum. This removed the momentary release that was observed for shots with a glue bond between the tantalum backer and the steel impactor (see Section 3.3). This bonding was performed by High Energy Metals, Inc. (Sequim, WA) and is typically used for the metallurgical joining of dissimilar metals with resulting bond strengths approaching the yield strength of each. The process uses the forces of controlled detonations to accelerate one metal plate into another at a slight angle, creating an atomic bond between the two materials usually with an interlocking surface structure. Explosive welding is considered a cold-welding process which allows metals to be joined minimizing the loss of their pre-bonded properties. Fig. 2.2 shows a metallographic cross-section of the material after bonding. The bonding layer between layer was determined to be less than 20um.

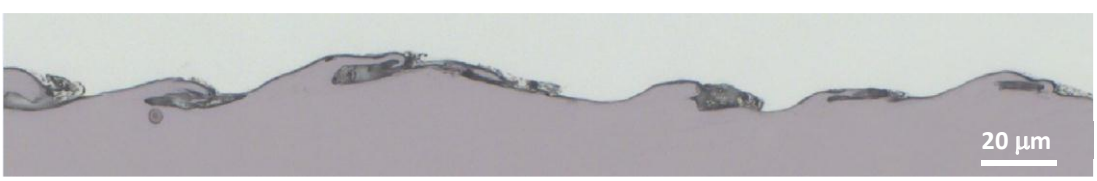

Figure 2.2. Cross-section of explosively-bonded interface between 2169 steel and tantalum.

Second, the free surface coupon was redesigned to increase useful read time prior to the intrusion of edge effects in the waveforms observed. The geometry used is detailed in Appendix A (Fig. A.6)

Finally, a set of four small LiF windows (and one large LiF window) was introduced to begin assessing whether transit times could be accurately measured explicitly. A map of the resulting target is shown in Fig. 2.3.

[1] See Section 4.1 for further discussion of characteristic bending and its effects on data interpretation.

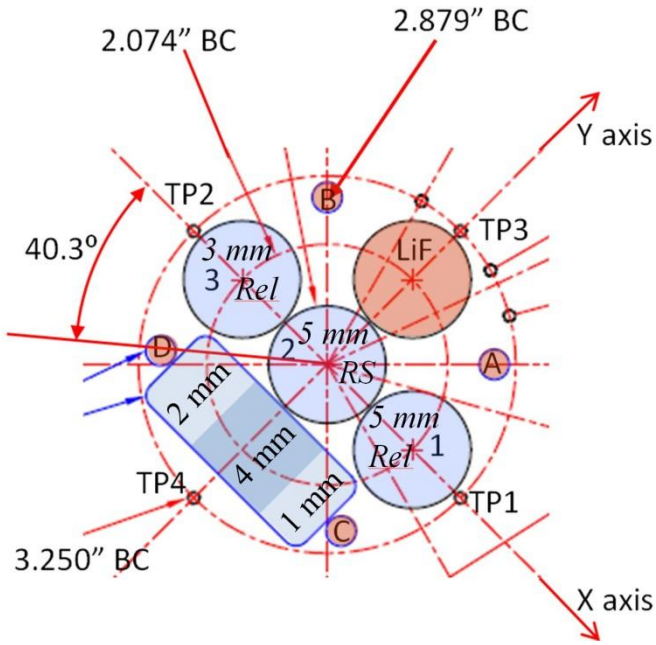

Figure 2.3. Standard target configuration (shots 6 – 8). Electrical shorting shot pins (velocity and tilt) are not shown. Samples are the same as in Fig. 2.1 except for the addition of a large LiF window ("LiF") and a larger rectangular stepped free-surface sample (regions of 1, 2, 4 mm thickness as indicated). As in Fig. 2.1, the samples along the X-axis were bonded to LiF windows (sapphire for shot 6). TP refers to electrical tilt pins, while A, B, C, D refer to 0.25" diameter LiF windows flush with the impact surface. BC is bolt circle diameter. View is toward the impact surface (i.e. from the bottom in the convention of Fig. 2.1).

2.2 Detailed specifications

Eight shots were conducted, giving Hugoniot conditions as listed in Table 2.1. The individual sample-by-sample Hugoniot and precursor conditions are tabulated in Appendix B (Table B.1). The calculation of these will be discussed further in Section 3.1.

The shot parameters for the first five shots are given in Table 2.2; for the last three, in Table 2.3. Sample diameters (samples 1 – 3) are all approximately 25.4 mm. The sample initial densities were 7.83 ± 0.02 gm/cm^3.

Table 2.1. Hugoniot conditions for windowed samples in 2169 steel experiments. See Tables B.1 and B.2 (Appendix B) for a complete tabulation. "NA" means the precursor was mostly or completely overdriven.

Shot #	Impact Vel (km/s)	Stress (GPa)	Strain	Shock Velocity (km/s)	Particle Vel. (km/s)	HEL (GPa)
SS1	0.520	9.97	0.053	4.84	0.260	0.74
SS2	1.005	20.3	0.096	5.23	0.502	0.95
SS3	1.242	25.9	0.114	5.41	0.621	1.18
SS4	1.713	38.3	0.150	5.71	0.856	NA
SS5	2.064	48.4	0.172	5.99	1.032	NA
SS6	0.693	13.6	0.069	4.94	0.347	1.58
SS7	1.304	27.3	0.120	5.44	0.652	1.25
SS8	2.010	46.8	0.169	5.95	1.005	NA

Sample 4 has a complicated stepped geometry (shown in perspective in Fig. 2.1). Details are given in Appendix A; the sample is divided into regions of thickness 1, 2 and 4 mm.

Table 2.2. Detailed shot parameters for 2169 steel experiments SS1 – SS5.

Shot #	SS-1	SS-2	SS-3	SS-4	SS-5
Impact Velocity (km/s)	0.520	1.005	1.242	1.713	2.064
Sample 1 thickness (mm) (release; windowed)	5.123	5.104	5.133	5.123	5.128
Sample 2 thickness (mm) (reshock; windowed)	5.126	5.123	5.110	5.118	5.123
Sample 3 thickness (mm) (release; windowed)	3.084	3.086	3.086	3.098	3.068
Sample 4 thickness 1 (mm)	1.036	1.044	1.034	1.024	1.036
Sample 4 thickness 2 (mm)	2.047	2.050	2.052	2.032	2.037
Sample 4 thickness 4 (mm)	4.069	4.072	4.061	4.059	4.072
VISAR VPF† Sample 1 (km/s)	0.0609	0.08365	0.08365	0.08365	0.08365
VISAR VPF† Sample 2 (km/s)	0.0402, 0.187	0.04804, 0.257	0.04804, 0.257	0.04804, 0.423	0.04804, 0.658
VISAR VPF† Sample 3 (km/s)	0.03497, 0.187	0.05521, 0.257	0.05521, 0.257	0.05521, 0.423	0.05521, 0.658
VISAR VPF† Sample 4(1) (km/s)	0.1235	0.3992	0.3992	0.542	0.844
VISAR VPF† Sample 4(2) (km/s)	0.1235	0.3992	0.3992	0.542	0.844
VISAR VPF† Sample 4(4) (km/s)	0.1235	0.3992	0.3992	0.542	0.844
Steel impactor thickness (mm)	1.034	2.083	2.070	1.515	1.530
Ta impactor backer thickness (mm)	6.350	6.342	6.350	6.342	6.300
Impactor backer material, thickness (mm)	TPX, 6.363	TPX, 6.363	TPX, 6.360	Al, 6.358	Al, 6.350
Window type (samples 1 - 3; sample 4 is free surface) (all windows are approx. 25.4 mm diameter and 12.7 mm thick)	Sapphire	LiF	LiF	LiF	LiF

†VPF is Velocity Per Fringe, a sensitivity setting for the VISAR interferometers. Samples with two values listed were monitored by two VISARs with different sensitivities, a method termed "dual delay" used to resolve ambiguities in the number of missed VPF constants to add at a rapid velocity excursion.

Table 2.3. Detailed shot parameters for 2169 steel experiments SS6 – SS8. The five LiF windows flush-mounted at the impact plane used velocity per fringe (VPF) values of 0.1076 – 0.5861 km/s.

Shot #	SS-6	SS-7	SS-8
Impact Velocity (km/s)	0.693	1.304	2.010
Sample 1 thickness (mm) (release; windowed)	5.009	5.009	5. 006
Sample 2 thickness (mm) (reshock; windowed)	5.004	5.006	5.009
Sample 3 thickness (mm) (release; windowed)	3.007	2.964	2.987
Sample 4 thickness 1 (mm)	0.975	0.980	0.980
Sample 4 thickness 2 (mm)	1.991	1.991	1.989
Sample 4 thickness 4 (mm)	3.995	3.990	3.983
VISAR VPF Sample 1 (km/s)	0.07829, 0.03497	0.3220, 0.04804	0.045698, 0.04804
VISAR VPF Sample 2 (km/s)	0.07829, 0.04020	0.3220, 0.05521	0.045698, 0.05521
VISAR VPF Sample 3 (km/s)	0.07829	0.3220	0. 045698
VISAR VPF Sample 4(1) (km/s)	0.3242	0.4872	0.75034
VISAR VPF Sample 4(2) (km/s)	0.3242	0.4872	0.75034
VISAR VPF Sample 4(4) (km/s)	0.3242	0.4872	0.75034

(continued on next page)

Table 2.3. (Continued)

Shot #	SS-6	SS-7	SS-8
Steel impactor thickness (most samples) (mm)*	1.6472	2.167	2.165
Steel impactor thickness (Sample 2) (mm)*	2.247	2.805	2.896
Ta backer thick (impacting Sample 2) (mm)	5.915	5.724	5.662
Impactor backer material, thickness (mm)	TPX, 6.526	TPX, 6.656	Al, 6.723
Window type (samples 1 - 3; sample 4 is free surface) (all windows are approx. 25.4 mm diameter and 12.7 mm thick)	Sapphire	LiF	LiF

*The process of machining the explosively bonded steel/Ta samples required removing an annulus of tantalum from a disk of the 2-layer impactor, then replacing it with TPX or aluminum to provide the release for all samples except for sample 2 at the center. Because of difficulties precisely locating the boundary during machining, the final impactor assembly had a slightly greater thickness of steel over the tantalum than elsewhere. We quantified this by identifying the release / reshock times-of-arrival on the waveforms and assuming the quasi-elastic sound speed at the Hugoniot state to be the same for reshock and release. The results of this calculation are incorporated into the values given here.

3.0 Impact Experiments - Results

3.1 Hugoniot and Loading Wave Structures

We begin with a discussion of the first 5 shots (SS1 – SS5). For symmetric-impact transmitted-wave experiments such as the present set, the Hugoniot state may be determined as follows. The time of impact (time when the shock enters the sample) is determined via the known wavespeed of the elastic wave toe in the present study, 5.75 km/s.

Shock Velocity: U_S = Sample thickness / transit time

Particle Velocity: $U_P = 0.5 * \text{Impact Velocity}$

Stress: $\sigma = \rho_0 * U_S * U_P$

Density: $\rho = \rho_0 * U_S / (U_S - U_P)$

The experimental values required are therefore: (1) the initial density of the sample (ρ_0), (2) the projectile velocity, (3) the sample thickness, and (4) the impact time relative to the observed waveform.

For the highest-velocity shot SS5, the elastic precursor was overdriven, so it was necessary to extrapolate the Hugoniot from the values determined in the other 4 shots.

The results are shown in summary form in Table 2.1 and plotted in $U_S - U_P$ space in Fig. 3.1 together with the results from earlier studies. Tables B.1 and B.2 (Appendix B) present the complete set of Hugoniot conditions, calculated accounting for 2-wave conditions as appropriate.

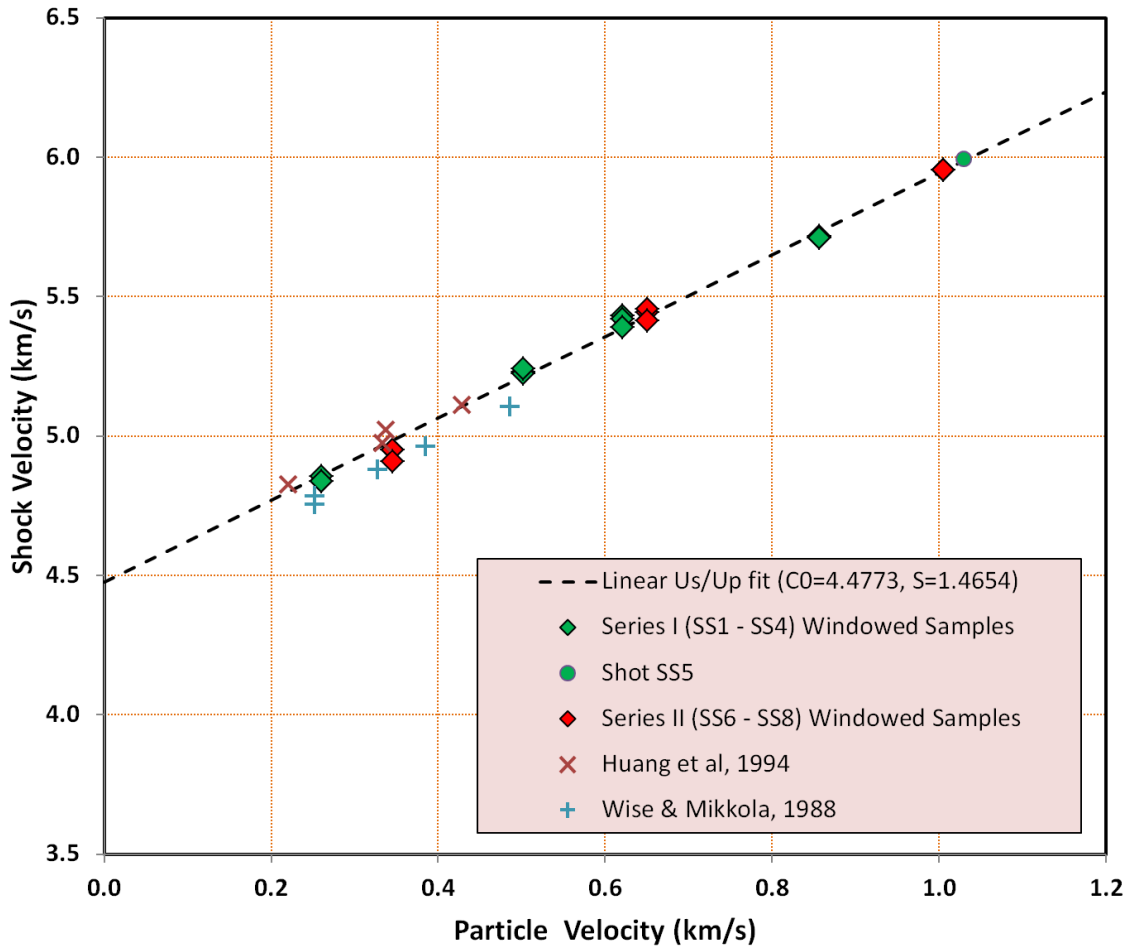

Figure 3.1. Hugoniot results for 2169 steel.

The wavespeeds for the (free-surface) stepped samples (1, 2, 4 mm thickness) are slightly lower than for the windowed samples, lowest for the thinnest samples. This is not surprising because a free surface will cause a release fan to propagate back into the sample when the initial loading arrives. This crossing effect is shown later in this report, in Fig. 4.1. The partially released material has a lower Lagrangian wavespeed than the fully compressed material, delaying the arrival of the later part of the wave at the surface. The effect on the waveforms is illustrated in Fig. 3.2. We have ruled out any role of edge effects in affecting the observed Hugoniot by performing 2-D CTH simulations (Appendix A) and noting that the effect persisted when the sample was redesigned to increase read time (see Section 2.1 and Appendix A).

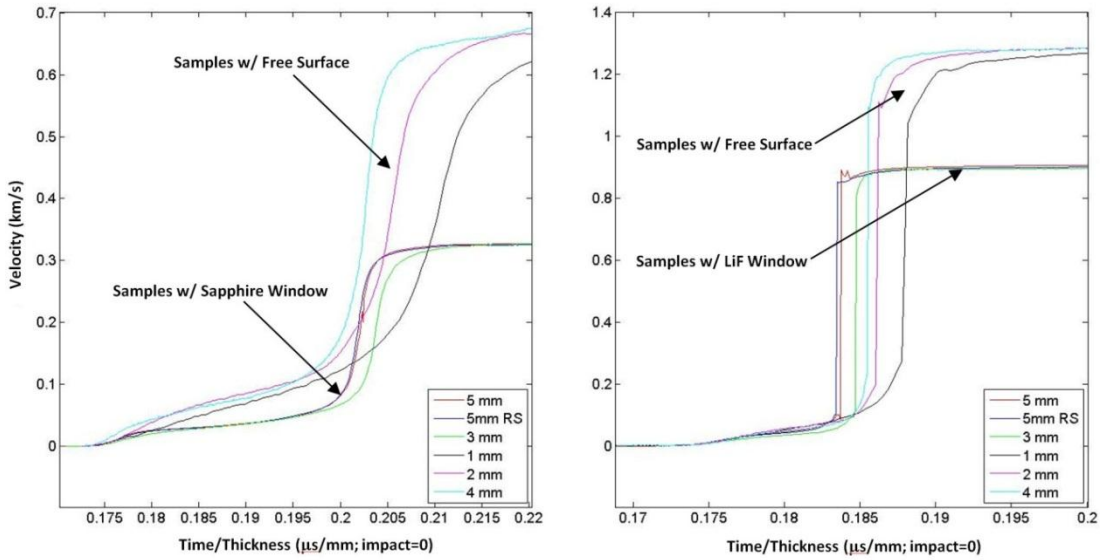

Figure 3.2. Scaled loading portions of waveforms for SS-6 (left) and SS-7 (right).

3.2 Free Surface Waveforms

Free surface samples were included in this series of experiments to provide model developers benchmark data free from modeling uncertainties of window materials (sapphire and LiF here; other materials have been employed as windows in other studies). As described above, these samples were subjected to direct impact by SS2169 steel (symmetric impact) backed by TPX or aluminum to provide a release wave following the initial loading. Representative waveforms are shown in Fig. 3.3; additional waveforms are shown in the Appendices (Figs. A.4, A.5, B.1). A discussion of read times prior to the arrival of edge effects may be found in Appendix A (Fig. A.2). Such effects were found to limit the read times for SS1 – 5. With the redesigned coupons used in SS6 – 8, longer read times were available.

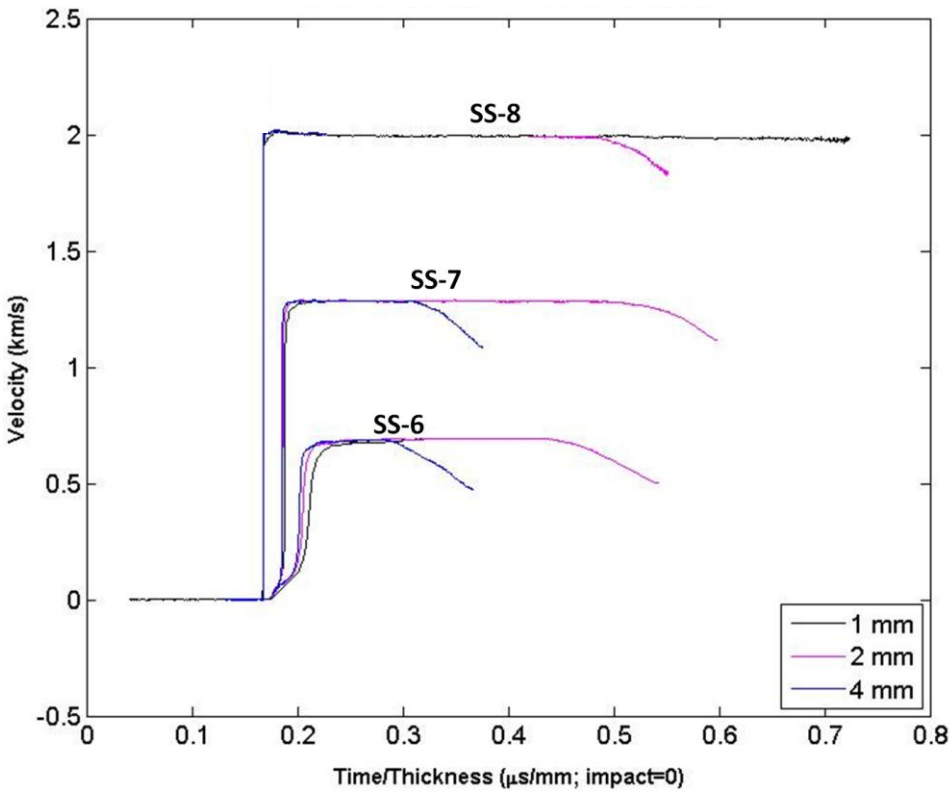

Figure 3.3. Scaled free surface waveforms for SS-6 - 8. The waveform durations shown are free from perturbations introduced by edge effects.

3.3 Waveforms for Windowed Samples

Three of the samples in each test were backed by LiF window (sapphire windows for the lowest-velocity tests, SS-1 and SS-6). The rationale for this was discussed in Section 2.1. Representative waveforms are shown in Fig. 3.4; see Appendix B for additional plots.

Two issues encountered in SS-1 (Fig. 3.5) were corrected for later shots. First, the thin impactor plate (~1 mm) resulted in overtake of the loading wave by the release wave propagating from the rear of the impactor in the thicker samples. This was subsequently solved with a thicker impactor for future tests. Second, the reload pulse was preceded by a pullback. This is due to a very thin glue bond between the steel impactor and the tantalum plate producing the reshock. In the steel, an elastic release marginally outruns the reloading wave, so the effect of a thin bond is amplified in the observed waveforms. Huang and Asay [2005] used a layer of indium in place of the epoxy to remove this pullback, and Chhabildas et al. [1982] reported such a pullback in beryllium. Our solution (see Section 2.1) was to use an explosive bonding process. This was implemented for shots SS-6 through SS-8.

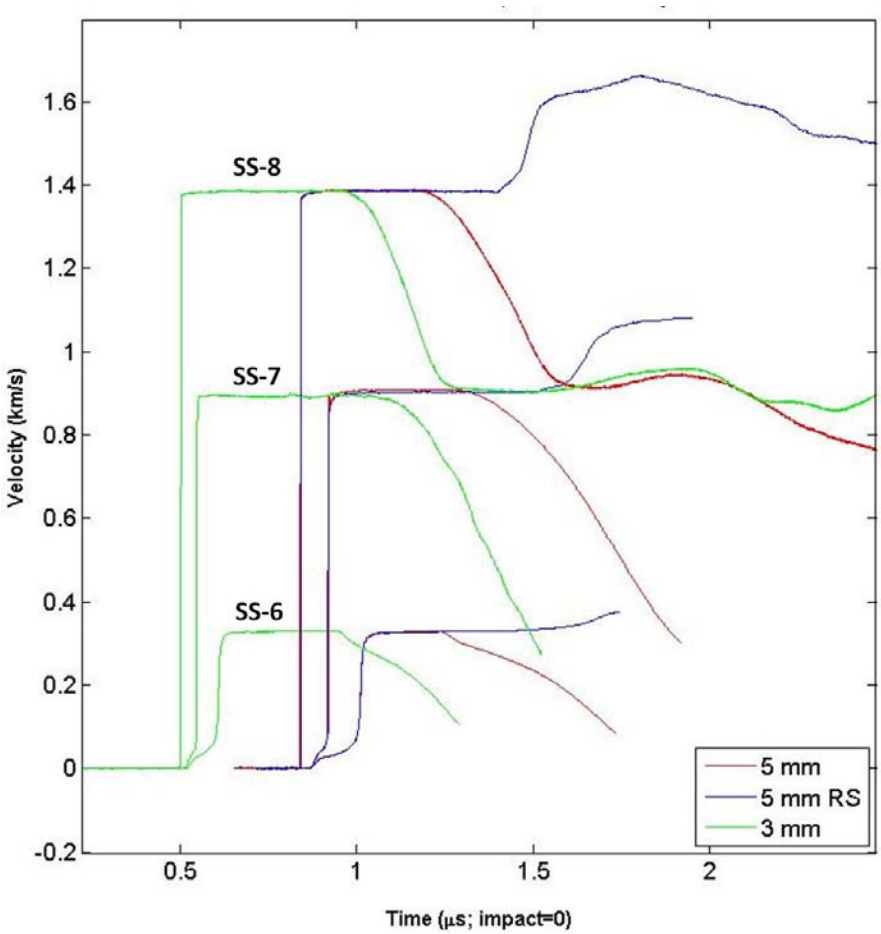

Figure 3.4. Windowed sample waveforms for SS-6 - 8.

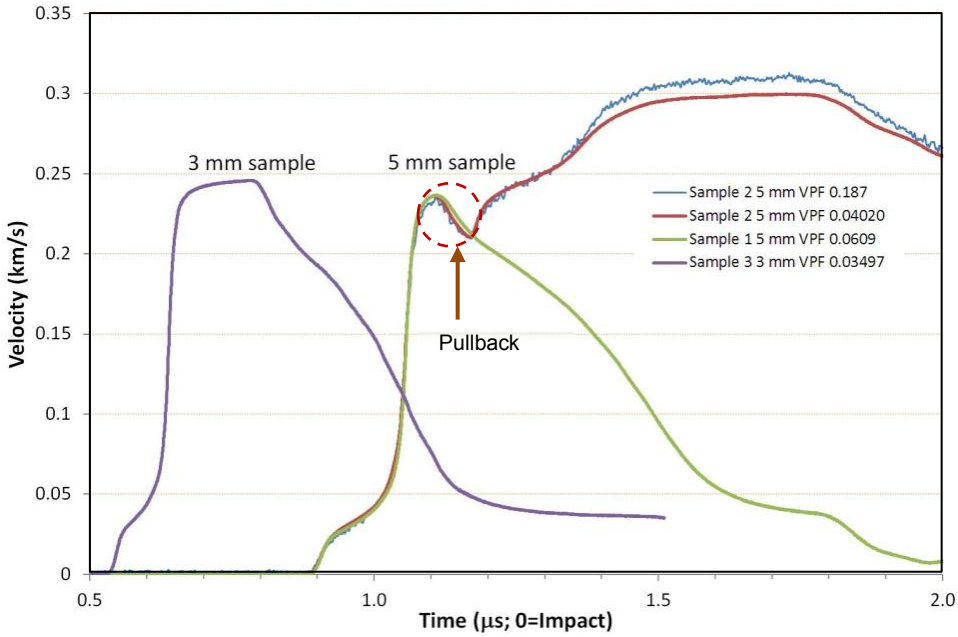

Figure 3.5. Shot SS-1 release and reshock waveforms (windowed samples). Initial loading is to 9.9 GPa.

The velocity histories for the windowed shock/release samples from all 5 tests are plotted together in Fig. 3.6. For shot SS-5, the elastic precursor is overdriven. The waveform timing for this shot therefore relies on the extrapolated steel Hugoniot (see Fig. 3.1), with a wavespeed of 5.99 km/s.

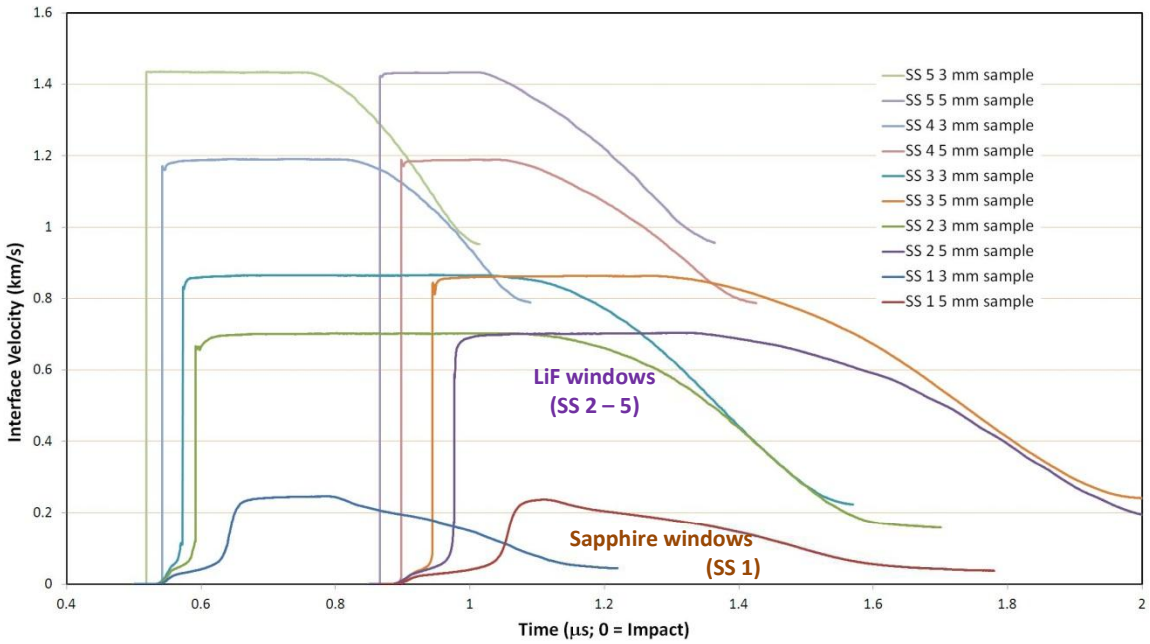

Figure 3.6. Velocity histories from windowed samples in shots SS1- SS5 subjected to compression/release cycle.

4.0 Impact Experiments: Hugoniot State Strength Interpretation

4.1 General Discussion of Strength in these Experiments

Consider the wave interactions present in this experiment. These are shown schematically in Fig. 4.1. In this figure, loading waves are generated by the impact, then propagate forward through the sample and back through the impactor. Next, these waves reflect as release waves from the LiF window and the TPX release material (respectively). The forward-running release fan travels to the sample/ window interface, giving the observed deceleration in the velocity history. The question is then how to deduce the material strength from the waveforms observed by VISAR at the sample/window interface.

The following brief discussion is based on Vogler and Chhabildas [2006], Huang and Asay [2005] and other sources.

It is first necessary to determine the relationship between wavespeed and longitudinal stress. This process requires the observed waveform as well as information about

component dimensions, material densities, impact velocity and loading curves of the window material. In some cases where the shock impedance of the window material ($C_0\rho_0$, where C_0 is the ambient sound speed; see also Section 2.1) is close to that of the sample, the process is relatively simple because the left-going fans shown in Fig. 4.1 are of small amplitude and do not greatly perturb the right-going fans. This is the case for shots SS-1 and SS-6, where the sapphire windows are close impedance matches to the steel samples. In other cases (e.g. LiF windows with steel samples), the impedance match is poor (a factor of 3) and the left-going fans do perturb the right-going fans. This is referred to as characteristics[1] bending, and is shown in exaggerated form in Fig. 4.1.

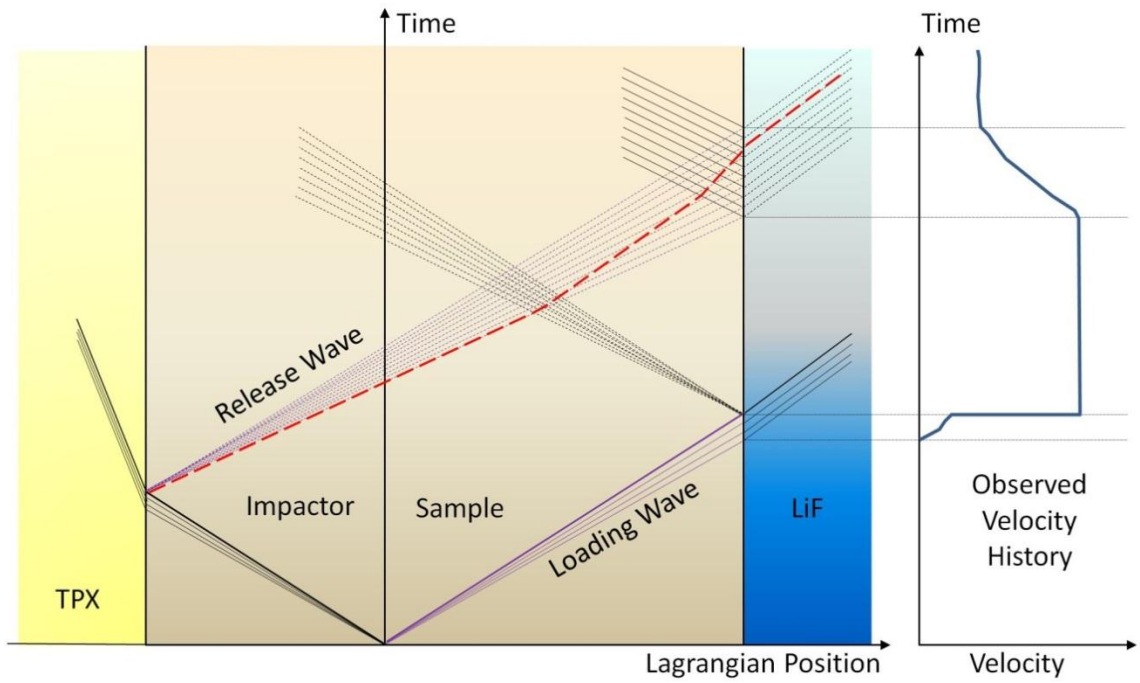

Figure 4.1. (Left) Position/time diagram of wave interactions for windowed release wave experiments. Portions of the wave motion used for the calculations are shown in purple. The release material is TPX for SS-1 through SS-3 and Al for SS-4 and SS-5. The window is LiF for SS2 – SS5 and sapphire for SS-1 (which sends a slight reshock back into the sample versus the release shown for the case of LiF). The dashed red line exaggerates the effect of characteristics bending upon meeting a release fan. (Right) Associated idealized velocity history measured by VISAR.

Several possible methods exist for correcting for characteristics bending, better calculating wavespeeds vs. stress. Three of these are:

- Iterative wavecode simulation of the experiment, with parameter optimization.
- A characteristics code tailored to this experimental configuration (accounting for all of the wave interactions shown in Fig. 4.1), and
- Using a linear function that maps the window velocity to the in-situ material velocity. This function (a "transfer function") is defined via a pair of simulations of the configuration in question, one using the window and the

[1] Characteristics are descriptors of wave progress introduced by Fowles and Williams [1970]. For intuition purposes they may be imagined to be wavelets making up the loading or release waves.

other replacing the window with additional sample material. For such a linear mapping to be valid, it must not greatly alter the particle velocities (a few %).

It is then possible to calculate relations between axial stress, strain, wavespeed, and material velocity (particle velocity).

From the particle velocity vs. wave speed representation, it is possible to calculate the shear stress for unloading and reshock experiments, and thus obtain an estimate of the material strength in the shocked state [Huang and Asay, 2005]. Consider a paired set of reshock/release experiments (Fig. 4.2(a)). It has been inferred from several different studies [Asay and Chhabildas, 1981; Huang and Asay, 2005; Reinhart and Chhabildas, 2003; Vogler and Chhabildas, 2006] that the material behaves according to the model presented in Fig. 4.2(c). This picture of strength assumes the material has some shear stress, τ_H, in the shocked state and is represented by point 2 ("state 2") in Figure 4.2(c). The yield surface associated with this strain is assumed to be symmetric and is characterized by the critical shear stress, τ_c. Then, as we shall see, the representation of Fig. 4.2(b) supplies a convenient space for computing Y, the material strength.

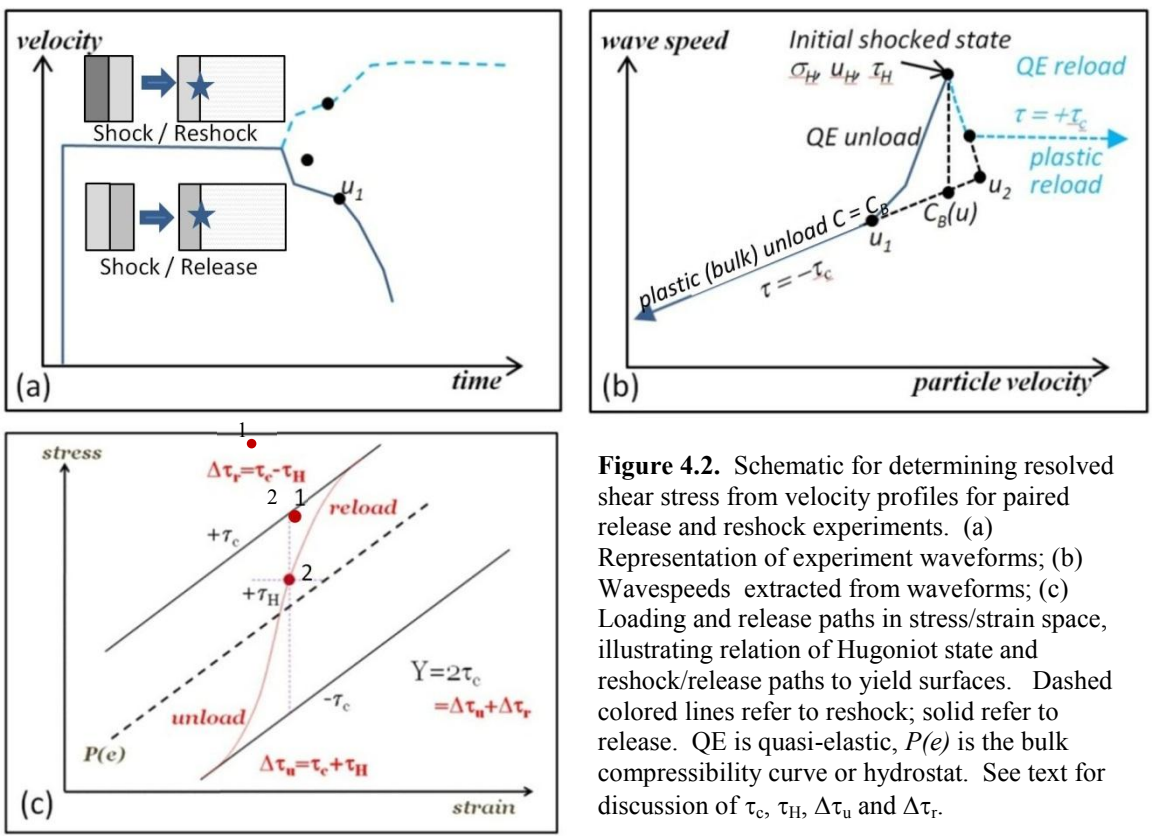

Figure 4.2. Schematic for determining resolved shear stress from velocity profiles for paired release and reshock experiments. (a) Representation of experiment waveforms; (b) Wavespeeds extracted from waveforms; (c) Loading and release paths in stress/strain space, illustrating relation of Hugoniot state and reshock/release paths to yield surfaces. Dashed colored lines refer to reshock; solid refer to release. QE is quasi-elastic, *P(e)* is the bulk compressibility curve or hydrostat. See text for discussion of τ_c, τ_H, $\Delta\tau_u$ and $\Delta\tau_r$.

For uniaxial strain shock loading, the resolved shear stress, τ, is defined as the difference between the principal stresses in the longitudinal (x) and transverse (y) directions:

$$2\tau = \sigma_x - \sigma_y , \qquad \text{Eq. 4.1}$$

and after yielding occurs is equal to the critical shear strength τ_c, ($\tau_c = 1/2\ Y$) , where Y is the current value of yield or flow strength at the corresponding stress and strain state. The relationship between shear stress, longitudinal stress and longitudinal strain for

uniaxial strain loading can be written as:

$$\frac{\partial \sigma}{\partial e} = \frac{\partial P}{\partial e} + \frac{4}{3}\frac{\partial \tau}{\partial e}, \qquad \text{Eq. 4.2}$$

where σ is the longitudinal stress, P is stress, and e is engineering strain defined as $1-\rho_0/\rho$. From the definitions of Lagrangian unloading or reloading wave speeds, c, and Lagrangian bulk wave speed [Lipkin and Asay, 1977], c_B, given below,

$$d\sigma_x = \rho_0 c^2 de \qquad \text{Eq. 4.3}$$

$$dP = \rho_0 c_B^2 de \ . \qquad \text{Eq. 4.4}$$

a differential equation can be developed for the resolved shear stress

$$d\tau = \frac{3}{4}\rho_0\left(c^2 - c_B^2\right)de \ ,$$

which applies to the response for unloading or reloading from the shock state. Integrating with respect to the particle velocity U_P gives:

Unload: $$\tau_c + \tau_H = -\frac{3}{4}\rho_0\int_{u_1}^{u_H}\left(c^2 - c_B^2\right)\frac{du}{c} \qquad \text{Eq. 4.5}$$

Reload: $$\tau_c - \tau_H = \frac{3}{4}\rho_0\int_{u_H}^{u_2}\left(c^2 - c_B^2\right)\frac{du}{c} \qquad \text{Eq. 4.6}$$

Then the total strength at the Hugoniot state is the sum of the resolved shear integrals for release and reshock:

$$Y = 2\tau_c = \Delta\tau_r + \Delta\tau_u \qquad \text{Eq. 4.7}$$

Returning to Fig. 4.2(c), since state 2 is assumed to be within the material's yield surface, an elastic response is expected for both unloading and recompression. The shear stress change from state 2 to plastic yielding at the $-\tau_c$ yield surface is $\Delta\tau = \tau_c + \tau_H$. Similarly, in reloading from state 2, the shear stress change from τ_H to the upper yield surface at $+\tau_c$ will be $\Delta\tau_r = \tau_c - \tau_H$. Earlier studies using only unloading for strength measurements have assumed that $\Delta\tau_r = \tau_c - \tau_H = 0$; i.e. the Hugoniot (state 2) is on the upper yield surface (state 1). If the states are indeed coincident, there is no error; if state 2 lies on the bulk curve $P(e)$, the strength deduced from the experiment is half of the correct value. All of the present experiments allow the calculation of $\Delta\tau_u$, while SS-6 through SS-8 also allow us to calculate $\Delta\tau_r$.

4.2 Impedance Matching Interpretation

Reduce, an explicit Lagrangian code written to infer stress-strain paths by comparing input and output wave profiles, was used to analyze the present suite of data to obtain relations between stress, strain, wavespeed and observed interface velocity. Inputs required for this program include the output velocity history, material density, sample thickness, shock entrance time into the sample, window type, and ramp duration of the loading input. Calculations were carried out to near the bottom of the initial release in the VISAR profile. The present analysis uses an iterative process to establish the sample shock impedance and wavespeed applicable to each timestep, then uses these to deduce the in-sample increments in stress, particle velocity and strain from the previous iteration.

It does not correct for characteristics bending within the sample (a small error for the two experiments with sapphire windows; slightly larger for the experiments with LiF samples; see red dashed line in Fig. 4.1). Later, another technique, which does account for characteristics bending, will be discussed.

For the present analysis, the evolution of the release (or reshock) wave through the combined thickness of the sample and impactor was used. Results from this analysis are shown in various spaces in Figs. 4.3 – 4.5. The stress – strain representation of Fig. 4.3 is useful for calculating loading/unloading hysteresis and therefore residual energy (and entropy) from the process of the shock/release loop (i.e. P×dV work). For this material in the pressure range 10 – 50 GPa, very little hysteresis is observed (the release is nearly down the Hugoniot).

The wavespeed – particle velocity representation (Figs. 4.4 and 4.5) is useful for calculating material strength, as discussed in Section 4.1. It is important to note that wavespeeds for the releases and reshocks are slightly underestimated in this calculation; this is due to not accounting for the characteristics bending illustrated in Fig. 4.1 for experiments using LiF windows (see Section 4.1).

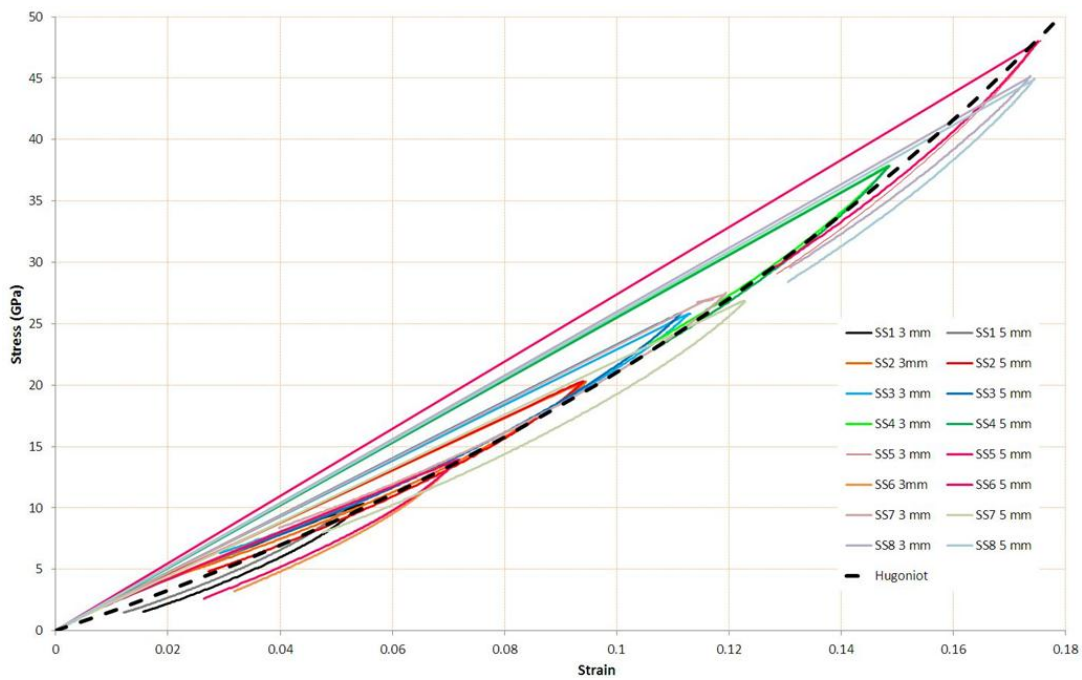

Figure 4.3. Stress-strain representation of loading / release paths for the 2169 steel. The loop is traversed in a clockwise direction.

Looking more specifically at experiments SS-6 through SS-8, the wavespeed vs. particle velocity mapping of the velocimetry data is shown in Fig. 4.5. We choose a representation of the plastic reload as shown in Fig. 4.6, then compute the resolved shear stress using Equations 4.5 and 4.6 for the unload (release) and load (reshock) paths, respectively. A similar plot for SS-1 – SS-5 (unload only) is shown in Appendix B. This plastic reload (linear in the wavespeed/particle velocity plane) is a simple approximation; there are better models available and analysis is ongoing.

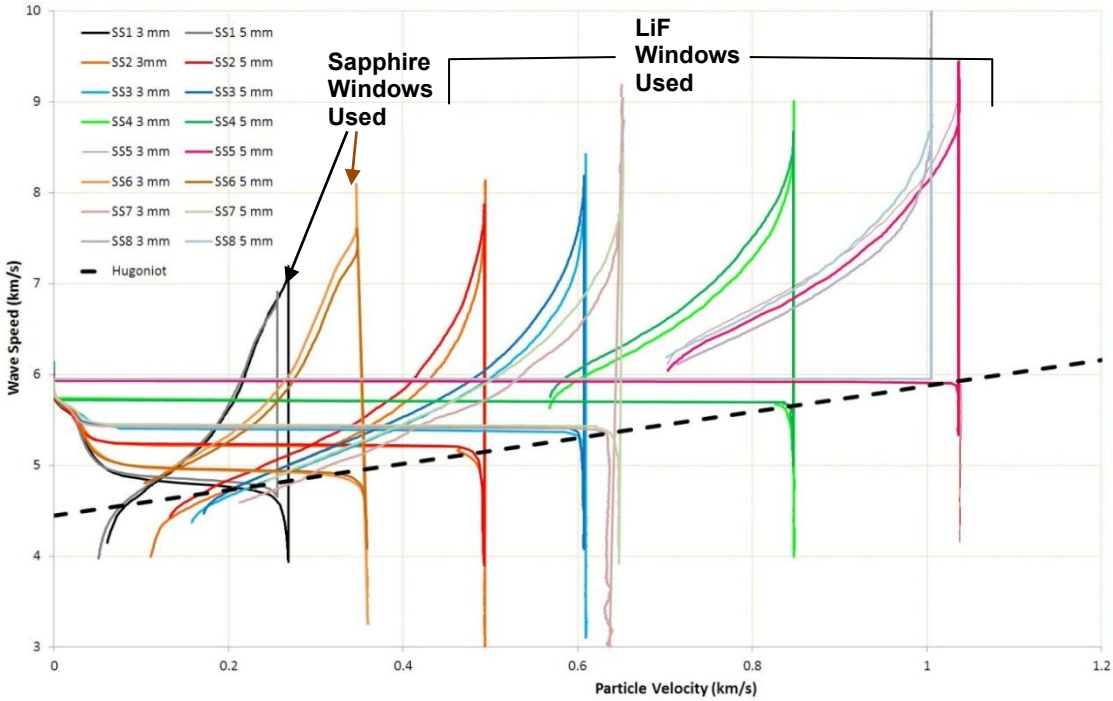

Figure 4.4. Wave speed – particle velocity representation of loading / release paths for the 2169 steel. Here the loop is traversed in a counterclockwise direction. Reshocks are omitted for clarity.

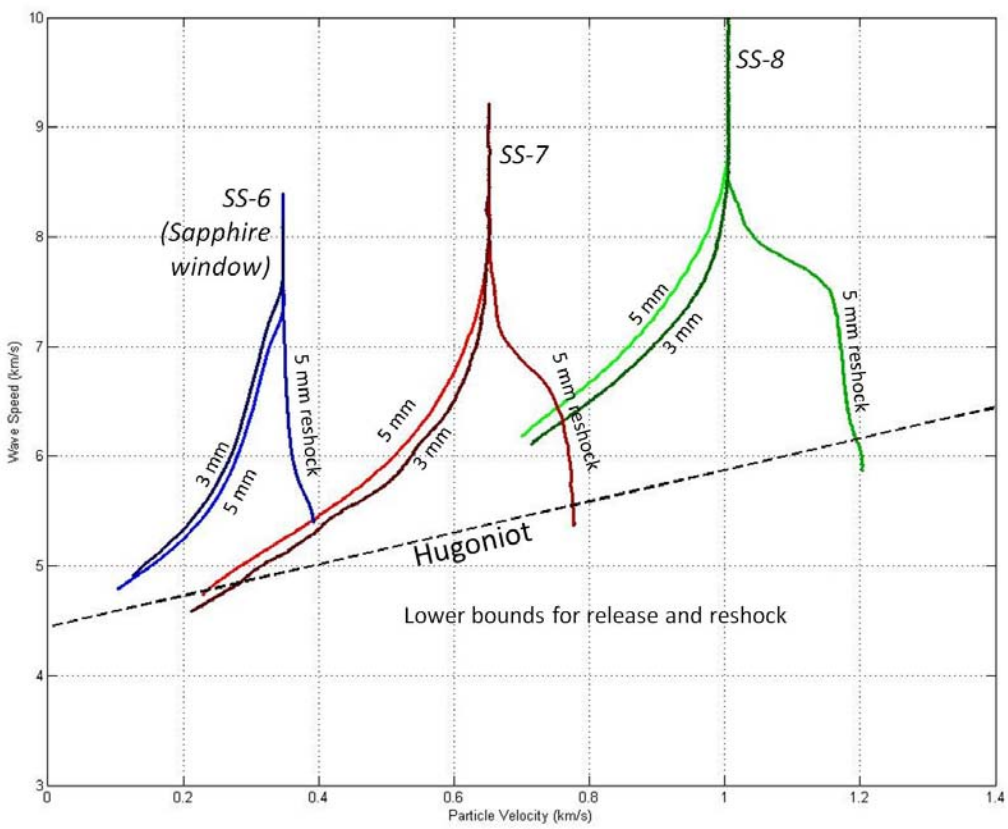

Figure 4.5. Wave speed – particle velocity representation of release and reloading paths for 2169 steel (shots SS-6 - SS-8). Initial loading portions are omitted for clarity.

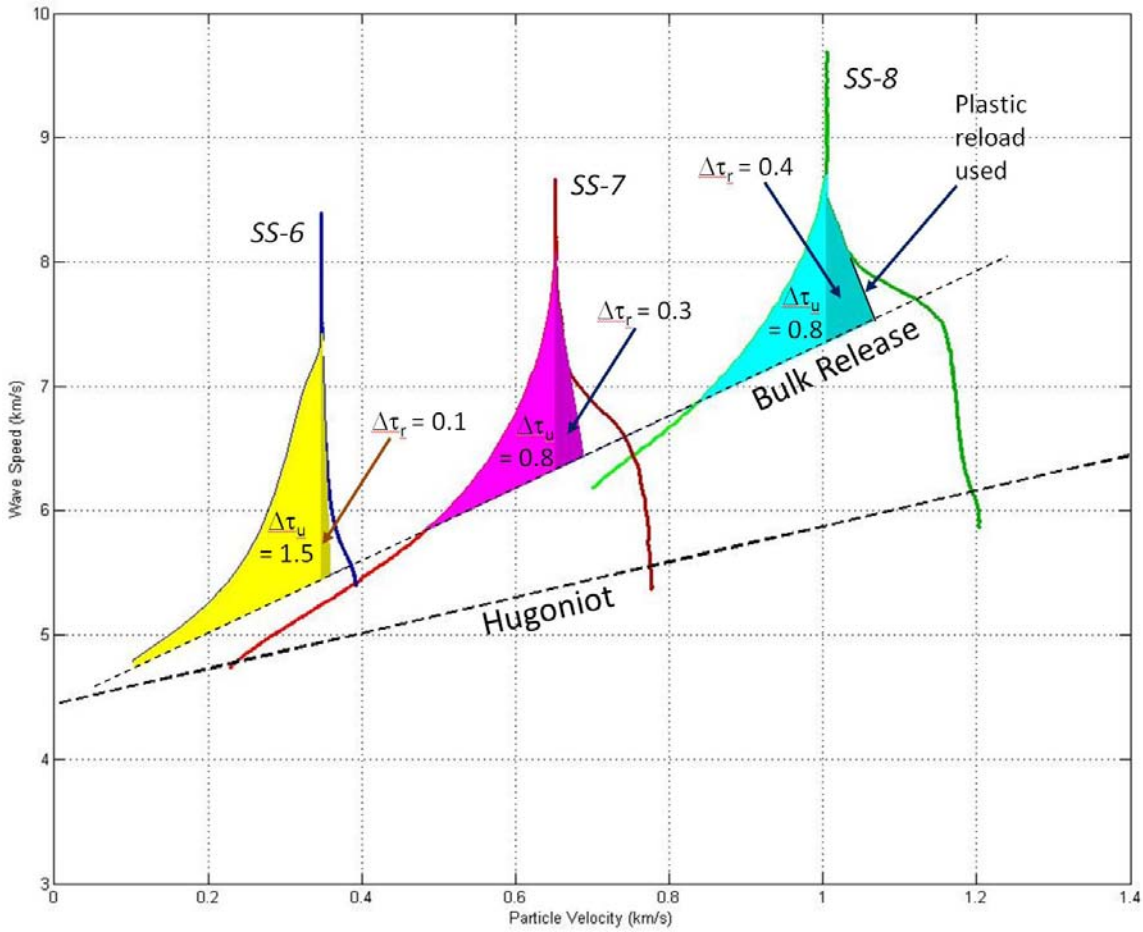

Figure 4.6. Integration spaces and values for $\Delta\tau_u$ and $\Delta\tau_r$ (in GPa) for shots SS6, 7, 8 (5 mm samples), using REDUCE analysis. Loading portions of the curves have been removed for clarity.

4.3 Transfer Function Interpretation

Several possible methods exist for correcting for the characteristics bending shown in exaggerated form in Fig. 4.1. The two methods used to greatest effect are the overtake method [McQueen, et al. 1982] and the characteristics method [Maw, 2004; Rothman et al, 2005]. The former, however, is only appropriate for determining the initial release wavespeed, while the latter assumes a unique one-to-one sound speed for a given stress or particle velocity. Thus, a symmetry breaking material response such as path and or rate-dependence, and entropy producing mechanisms such as plastic work may cause errors in the analysis. For ramp compression on lead, these errors appear to be much less than other experimental uncertainties [Rothman and Maw, 2006], while for shock and release experiments on copper the errors were incorporated into the overall experimental uncertainty [Rothman, et. al., 2012], and, again, appear to be relatively small. To avoid these issues, a new technique which does not contain any inherent assumptions about material behavior has been developed. This new methodology is based on basic systems control theory, and, as such, has been deemed the transfer function approach. A cartoon illustrating the flow of information in the technique is shown in Fig. 4.7.

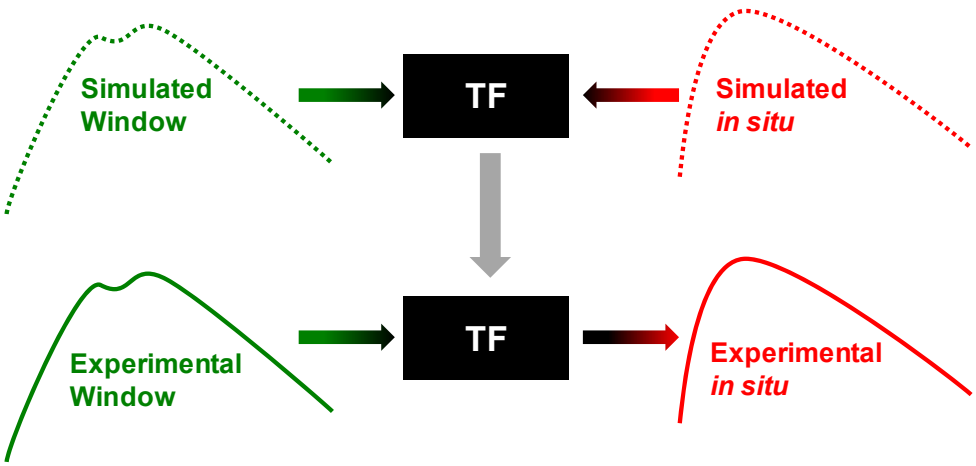

Figure 4.7. Flow of information in the transfer function interpretation.

As shown in the top of the cartoon, the problem begins with a numerical simulation of the experiment in question. The principal idea is that the hydrocodes are very good at handling wave interactions for a complex material response. To evaluate the effect of the wave interactions due to the window, an *in situ* simulation is run. This is an identical simulation except the window is replaced with an infinite block of target material. Thus, for the same set of loading conditions and material definitions, the particle velocity –time profile at the window and at the same *in situ* Lagrangian position is obtained. Next, a mapping between these profiles can be defined using controls theory. For a time-invariant linear system, the signals may be related through a convolution as

$$u_{in\ situ}^{simulated}(t) = u_{window}^{simulated}(t) * tf(t), \qquad \text{Eq. 4.7}$$

where *tf* is the transfer function. The transfer function is perhaps best thought of as a "black box" in which the window velocity is fed into the box (transfer function) and the output is the *in situ* velocity. The system is clearly time-invariant since timing is purely relative and ultimately arbitrary (u(t) = u(t-T)). Linearity, however, is an important assumption and will be discussed in further detail, but ultimately depends on how well the simulation represents the actual experiment.

For this type of system, the transfer function can easily be solved in the frequency domain since the convolution becomes a multiplicative operator in this space:

$$TF(\omega) = \frac{U_{in\ situ}^{simulated}(\omega)}{U_{window}^{simulated}(\omega)}, \qquad \text{Eq. 4.8}$$

where U(ω) is the fast Fourier transform (FFT) of the velocity – time profile, u(t). Next, the wave interactions in the simulation are assumed to be a close representation of the actual experiment, so the same transfer function is used to map the experimental window velocity into an experimental *in situ* velocity. Again, this is easily done in the frequency domain, and ultimately the inverse FFT of the experimental *in situ* velocity-frequency

profile results in waveform of interest.

$$U_{in\ situ}^{experimental}(\omega) = U_{window}^{experimental}(\omega) \cdot TF(\omega)$$
$$u_{in\ situ}^{experimental}(t) = FFT^{-1}\left[U_{in\ situ}^{experimental}(\omega)\right] \qquad \text{Eqs. 4.9}$$

As an example of this type of analysis, SS7 will be discussed in detail. The experiment was modeled using a Mie-Gruneisen EOS based on the Hugoniot determined in Section 3 and a Gruneisen coefficient of 1.5. A modified 304 stainless steel Steinberg-Guinan strength model [Steinberg, 1996] was used to calculate the yield surface, but the constitutive response was modified to include quasi-elasticity through the use of an effective shear modulus. The effective modulus takes the form

$$G_{eff} = G\left[1 - \left(\frac{\varepsilon^* - \varepsilon}{\varepsilon^* - \varepsilon_t}\right)^p\right], \qquad \text{Eq. 4.10}$$

where G is the original shear modulus, ε^* is the stain at which QE begins, ε_t is the self-consistent transition strain which gives the correct yield stress, and p is a fitting parameter used to modify the overall nature of the rate of quasi-elasticity which generally falls between 0.25 and 2. The results of the simulations compared to the experimental data are shown in Fig. 4.8. It should be noted that this model may not be physically relevant, and is simply used to simulate waveforms which are qualitatively similar to what is observed in the experiment, which is all that this technique requires. Ultimately, if the something close to the proper wave interactions can be simulated, the resulting transfer function should be good enough to map the experimental profile, which certainly contains all of the relevant physics, to a realistic *in situ* velocity.

While the window velocity simulations are an imperfect match, they are still within 5% of the experimental VISAR measurements. As mentioned previously, the linear nature of the theory suggests that slight experimental perturbations from the simulations will be mapped accurately through the transfer function, which can be seen in the qualitative nature of the profiles in Figure 4.8. As such, it is expected that perturbations of this order will not introduce significant errors, with recent work on ramp compression suggesting the overall uncertainties are dominated by the experimental errors with little influence from the systematic errors in this methodology. In fact, very reasonable results have been obtained for perturbations closer to 25%.

The effect of correction for characteristics bending is evident in the increased wavespeeds from the Reduce results for SS-7 and SS-8 (Fig. 4.9). With the sapphire window shot (SS-6), there is very little change because the sapphire is a fairly good shock impedance match with the steel.

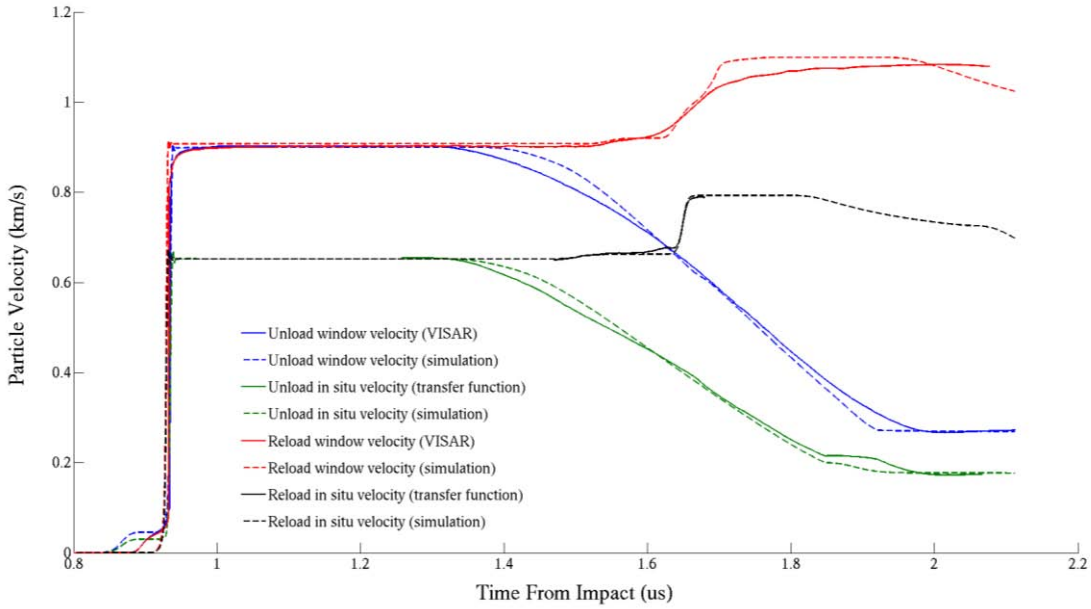

Figure 4.8. Transfer function analysis for SS7. The simulations are shown as dotted lines, while experimental curves are given by their solid counterparts. The window results in higher measured velocities, and significantly alters the apparent wavespeeds.

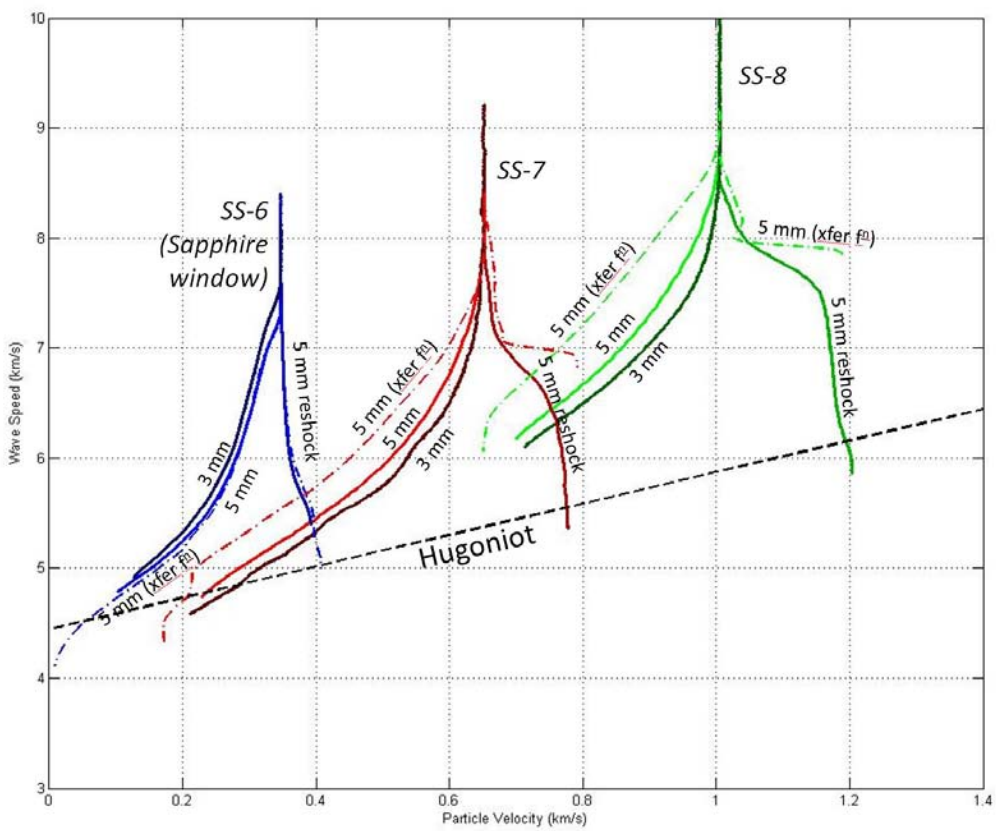

Figure 4.9. Transfer function results for SS6 – 8 (wavespeed/particle velocity space), juxtaposed on Reduce results

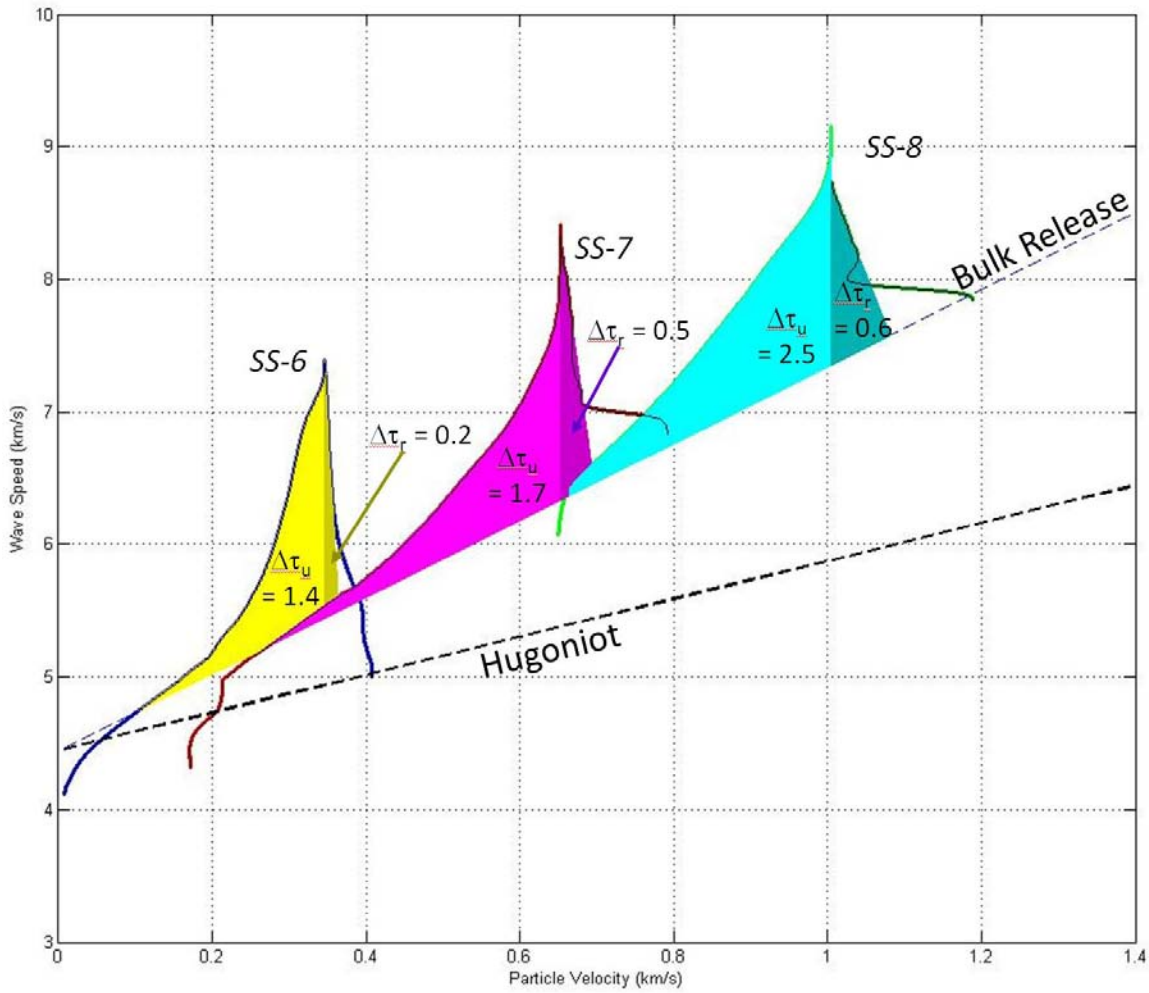

Figure 4.10. Integration spaces and values for $\Delta\tau_u$ and $\Delta\tau_r$ (in GPa) for shots SS6, 7, 8 (5 mm samples), using transfer function analysis. Loading portions of the curves have been removed for clarity.

The total resolved strength *Y* can be estimated from the wavespeed – particle velocity integrations (eqs. 4.5 and 4.5) is summarized in Fig. 4.11 for the three shots including both release and reshock. The transfer function method shows a clear trend of increasing strength; since this method accounts for characteristics bending, we consider this more credible than the Reduce results. Neglecting this probably has little effect on SS-6 because of the sapphire window; for SS-7 and SS-8 (LF windows), it is believed to cause an under-calculation of the release and reshock wavespeeds, and hence of the resolved shear stress. Therefore we have assigned a large upside uncertainty for these two points. These values are tabulated as well in Table 4.1.

Table 4.1. Strength values at Hugoniot conditions for tests SS-6 – SS-8. All values in GPa. Uncertainties in last digits or ranges are given in parentheses.

Shot	σ_H	Transfer Function			Reduce		
		$\Delta\tau_u$	$\Delta\tau_r$	Y	$\Delta\tau_u$	$\Delta\tau_r$	Y
SS-6	13.2	1.36	0.17	1.53(31)	1.46	0.12	1.58 (1.27 – 1.90)
SS-7	27.5	1.74	0.47	2.22(44)	0.85	0.30	1.14 (0.9 – 3.2)
SS-7	46.4	2.45	0.57	3.02(60)	0.83	0.41	1.25 (1.0 – 3.9)

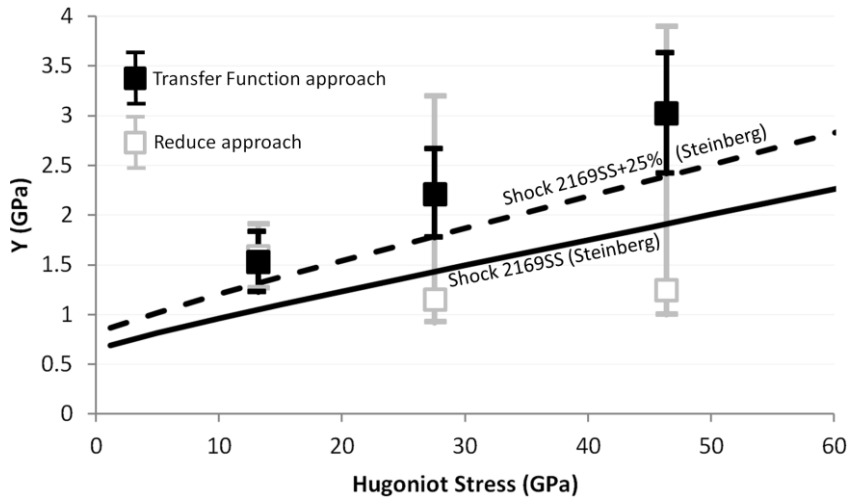

Figure 4.11. Yield strength Y = $\Delta\tau_u + \Delta\tau_r$ for SS-6, 7, 8. Curves are deduced from Steinberg [1996] modeled for ramp loading, and include approximate correction to shock and (dashed curve) addition of 25% as an eye guide (see text).

For SS-6 through SS-8, the average value of $\Delta\tau_u$ / ($\Delta\tau_u + \Delta\tau_r$) is 0.82; therefore the Hugoniot in this general region is ~80 - 84% of the distance from the lower yield surface to the upper yield surface. This means that strength from analyses using the release data alone to measure strength needs to be corrected upward by ~25%.

As an eye guide only, this correction is applied to the calculated curve in Fig. 4.11. It appears that the strength measured here is ~40% greater than the unmodified Steinberg curve. We emphasize that the curve shown here may not correspond to the anneal or cold-work state of the present samples.

Hence, the overall strength of the 2169 steel increases from ~1.6 GPa at 13 GPa to ~3 GPa at 47 GPa. The scatter of these points suggests a 15 – 20% uncertainty in individual strength measurements. These strength values are only slightly lower than values derived from manganin gage deviatoric stress measurements recently published by Whiteman and Millett [2012] (Y ~ 1.7 GPa at a 10 GPa axial stress level). Their samples were from a hot-rolled, nitrogen-strengthened, austenitic stainless steel with an average grain size of ~90 microns (roughly twice that for the present samples). Other than potential sample preparation issues, there are at least two reasons for such a difference:

1. The deviatoric stress measurements apply to single stress levels, while the present uniaxial strain measurements are gauges of phenomena occurring over a range of axial stress levels (e.g. a release experiment is sensitive to properties over progressively lower stresses as the release progresses).
2. The transfer function studies suggest that the releases in the present experiments remained quasi-elastic over the entire interval of the release, that the lower yield surface was never reached, and therefore that the present strength results are underestimates.

5.0 Summary

We have conducted a uniaxial strain study of 2169 stainless steel over the stress range 10 – 50 GPa, using a multi-sample configuration in which each shot provides release and reload measurements for windowed and free-surface samples. For the reload measurements, a novel explosive-bonding process was used in constructing the impactors; this removed the pullback signal preceding the reload seen in earlier studies caused by an infinitesimal glue bond.

The principal conclusions from this study are:

(1) The Hugoniot is nearly linear, and shows no sign of the Fe $\alpha \rightarrow \varepsilon$ phase transition. The releases do not show a clear sign of a phase transition, such as a large deviation from releasing down the Hugoniot.

(2) The Hugoniot points measured with the stepped samples (free surface) are consistently softer than those measured with the windowed samples, with the thinnest samples showing the lowest wavespeeds. This is the opposite of what would be expected from dislocation mechanics for nonsteady waves, and may also related to characteristic bending.

(3) Strength is an increasing function of stress over the interval 10 – 50 GPa for this steel, and is ~40% greater than that predicted by the Steinberg model for this material.

(4) Earlier studies employing release, but not reloading, underestimate the material strength by 20 – 25%.

Future work to be considered would include releasing the material to as close to zero as practical (requiring a sapphire window to avoid spallation and wave stagnation), explicitly controlling the impactor thickness for reshock experiments, conducting an additional test at ~60 GPa, and diamond anvil experiments to better constrain the hydrostat.

References

Asay, J. R. and Chhabildas, L. C., Determination of the shear strength of shock compressed 6061-T6 aluminum, in Shock Waves and High-Strain-Rate Phenomena in Metals: Concepts and Applications, edited by Meyers, M. A. and Murr, L. E., Plenum, pp. 417-431, 1981.

Barker, L. M. and Hollenbach, R. E., Shock-wave studies of PMMA, fused silica and sapphire, J. Appl. Phys., 41, 4208-4226, 1970.

Chhabildas, L.C., Wise, J.L., and Asay, J.R., Shock and release behavior of beryllium, pp. 422-426 in Shock Waves in Condensed Matter – 1981, Nellis, W.J., Seamanm L. and Graham, R.A. (eds), American Institute of Physics, 1982.

Fowles, R. and Williams, R. F. Plane stress wave propagation in solids, J. Appl. Phys., 41, 360-363, 1970.

Furnish, M.D. and Chhabildas, L.C., Dynamic material properties of refractory materials: molybdenum, pp. 229 – 240 in high strain rate behavior of refractory meals and alloys, Asfahani, R., Chem E. and Crowson, A. (eds), TMS, 1992.

Hertel, E. S. Jr.; Bell, R. L.; Elrick, M. G; Farnsworth, A. V.; Kerley, G. I.; McGlaun, J. M.; Petney, S. V.; Silling, S. A.; Taylor, P. A.; and Yarrington, L., CTH: A Software Family for Multi-Dimensional Shock Physics Analysis, Proceedings of the 19th International Symposium on Shock Waves, Volume 1, pages 377-382, Marseilles, France, 26-30 July 1993.

Huang, H., and Asay, J.R. Compressive strength measurements in aluminum for shock compression over the stress range of 4-22 GPa. J. Appl. Phys., 98, pp. 033524, 2005.

Huang, S., Jin, X., Li, Z., Wang, X. and Guan, K, Experimental measurements of 2169 stainless steel under dynamic loading, pp. 1083-1086 in Schmidt, S.C., Shaner, J. W., Samara, G. A. and Ross, M., High Pressure Science and Technology – 1993, American Institute of Physics Press (AIP Conference Proceedings 309), 1984.

Lipkin, J. and Asay, J. R., Reshock and release of shock-compressed 6061-T6 aluminum, J Appl Phys, 48, 182-189, 1977.

Maw, J., A characteristics code for analysis of isentropic compression experiments, pp. 1217-1220 in Shock Compression of Condensed Matter – 2003, Furnish, M.D., Gupta, Y.M. and Forbes, J. W. (eds), AIP Press, 2004.

McQueen, R. G., Hopson, J. W., and Fritz, J. N., Optical technique for determining rarefaction wave velocities at very high pressures, Rev. Sci. Instr., 53, 245-250, 1982.

Reed, B. W., Stolken, J. S., Minich, R. W. and Kumar, M., A unified approach for extracting strength information from nonsimple compression waves. Part I: Thermodynamics and numerical implementation, J. Appl. Phys., 110 (11), 113505, 2011a.

Reed, B. W., Patterson, J. R., Swift, D. C., Stolken, J. S., Minich, R. W. and Kumar, M., A unified approach for extracting strength information from nonsimple compression waves. Part II: Experiment and comparison with simulation, J. Appl. Phys., 110 (11), 113506, 2011b.

Reinhart, W. D. and Chhabildas, L. C., Strength properties of Coors AD995 alumina in the shocked state, Int. J Impact Eng, 29, 601-619, 2003.

Rothman, S. D., Davis, J.-P., Maw, J., Robinson, C. M., Parker, K., and Palmer, J., Measurement

of the principal isentropes of lead and lead-antimony alloy to ~ 400 kb by isentropic compression, J. Phys. D, 38, 733-740, 2005.

Rothman, S. D. and Maw, J., Characteristic analysis of isentropic compression experiments (ICE), J. de Phys. IV, 134, 745-750, 2006.

Rothman, S. D., Edwards, R. J., Vogler, T. J. and Furnish, M. D., Inferring the high-pressure strength of copper by measurement of longitudinal sound speed in a symmetric impact and release experiment, pp. 104-107 in Shock Compression of Condensed Matter – 2011, Elert, M. L., Buttler, W.T., Borg, J. P. Jordan, J. L. and Vogler, T. J. (eds.), AIP Press, 2012.

Setchell, R. E., Index of refraction of shock-compressed fused silica and sapphire, J. Appl. Phys., 50, 8186-8192, 1979.

Steinberg, D. J, Equation of state and strength properties of selected materials, LLNL report, UCRL-MA-106439 (change 1), 1996.

Vogler, T. J., and Chhabildas, L. C., Strength behavior of materials at high pressures, Int. J. Impact Engrg., 33, 812-825, 2006.

Whiteman, G. and Millett, J.C.F., Shear stress measurements in stainless steel 2169 under 1D shock loading, Experimental Mechanics 52:265-273, 2012.

Wise, J. L. and Chhabildas, L.C., Laser interferometer measurements of refractive index in shock-compressed materials, p. 441-454 in Gupta, Y.M. (ed), Shock Waves in Condensed Matter, Plenum, 1986.

Wise, J. L. and Mikola, D. E., Hugoniot and wave-profile measurements on shock-loaded stainless steel (21Cr-6Ni-9Mn), pp. 261-264 in Schmidt, S.C. and Holmes, N.C., Shock Waves in Condensed Matter – 1987, Elsevier, 1988.

Appendix A: Further Discussion of Target Geometries (Including the Stepped Samples)

For shots SS1 – SS5, the configuration of Fig. A.1 was used. Tilt and velocity pins were arranged on two circle patterns. Circle A (the primary shot diagnostic circle) included the velocity pins and one set of four electrical shorting tilt pins. Circle B, around the stepped free-surface target, included four additional tilt pins. The stepped sample piece is shown in detail in Fig. A.2.

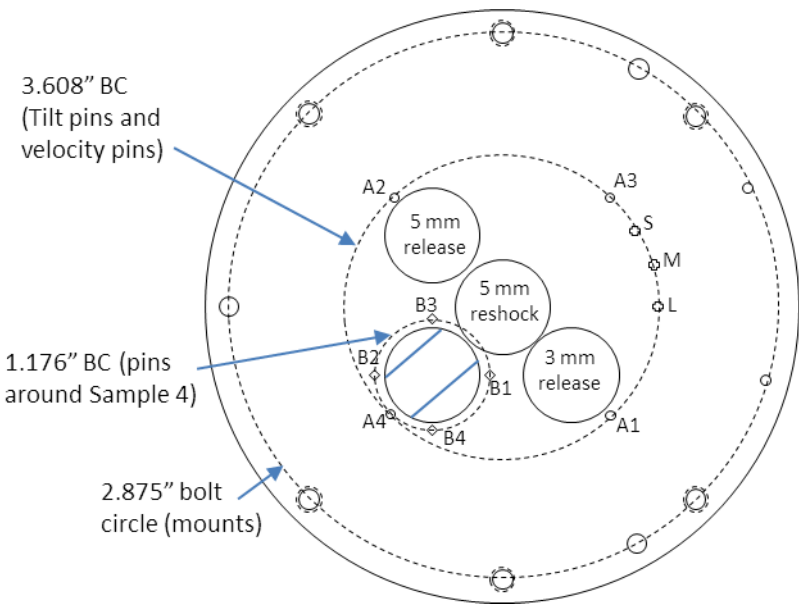

Figure A.1. View of target plate from projectile. S, M, L refer to velocity pins (short, medium, long). A1 – A4 are primary tilt pins; B1 – B4 are supplemental tilt pins. The view is from the front of the target (i.e. looking from the bottom in Fig. 2.1).

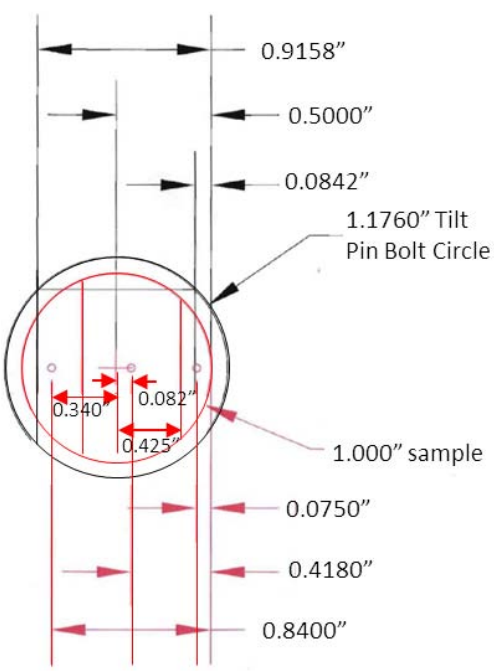

Figure A.2. Top view of free-surface sample (shots SS1 – SS5). Dimensions are in inches.

A concern with this design of stepped sample is whether it is susceptible to edge effects. We performed 2-dimensional modeling of this target with the Eulerian wavecode CTH [Hertel, 1993]. The geometry used is shown in Fig. A.3, and is conservative in the sense that it only accounts for edge effects originating from the sides at 3:00 and 9:00 in the orientation of Fig. A.2. Dimensions and impact velocity were chosen to match test SS-2. The steel model used was MGR 21-6-9_SS; the PMMA model used was MGR PMMA. A strength of 0.68 GPa (slightly low in view of later results), a Poisson ratio of 0.33 and a melt temperature of 0.205 eV were assumed.

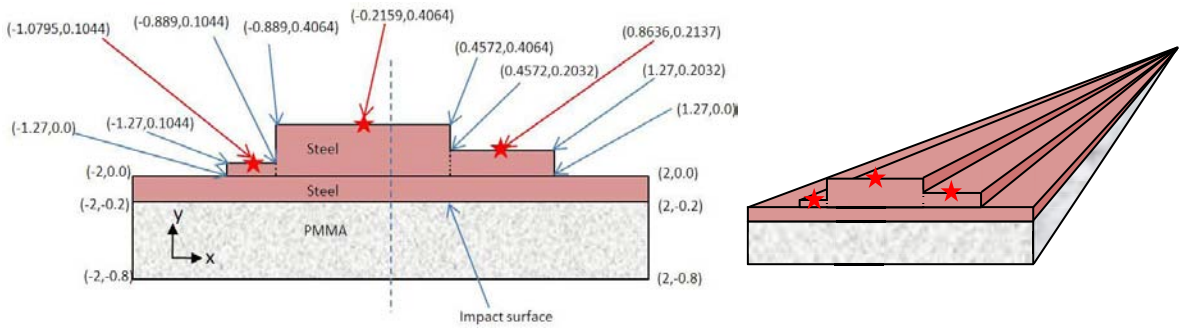

Figure A.3. Configuration used in CTH simulations of stepped (free surface sample). Stars mark the spots monitored by VISAR.

The velocity components of the VISAR spots in the ŷ direction (normal to the impact surface) were calculated, then the simulation was redone with all x dimensions increased by a factor of 10 to eliminate edge effects. The results are shown in Fig. A.4. Edge effects perturb the calculated waveforms beginning immediately after the shock arrival for the 1 mm thick sample, and only slightly later for the 2 and 4 mm thick samples.

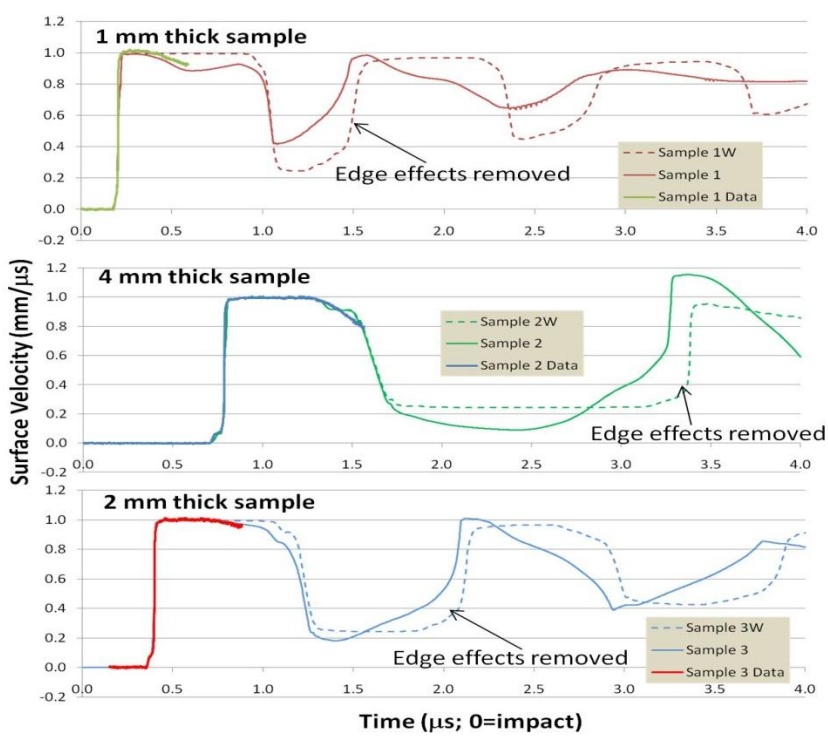

Figure A.4. Results of CTH simulations of free-surface samples for Test SS-2, juxtaposed on experimental waveforms

The experimental waveforms for shot SS-3 are shown in Fig. A.5; for the free-surface waveforms for the remainder of the shots, see Appendix B.

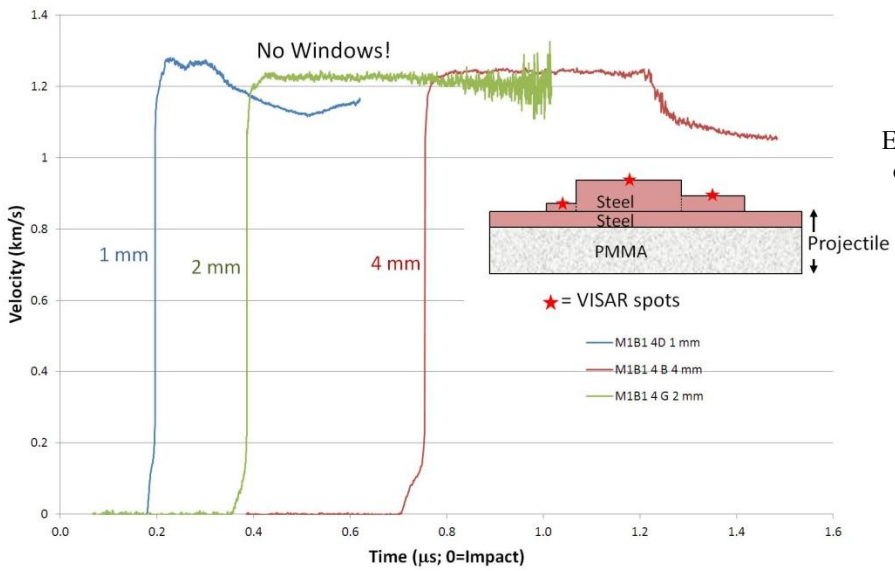

Figure A.5. Experimental waveforms of free surface samples for Test SS-3.

To mitigate these edge effects, the stepped samples were redesigned as shown in Fig. A.6.

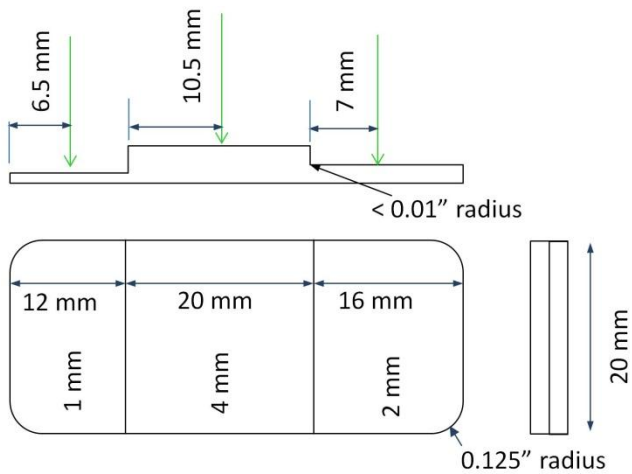

Figure A.6. Design of stepped sample used in tests SS6 – SS8. Vertical arrows at top correspond to VISAR probe positions.

We addressed a similar edge-effect question for the disk-shaped samples, of interest because the experiment design evolved to use thicker samples (5 mm) and impactors (2 mm). As before, we used CTH to model the experiments with the nominal aspect ratios, then again with the lateral dimensions increased by 10x to remove edge effects from the central areas of the samples. The results for release and reshock experiments show that edge effects do not appear to perturb the observed waveforms during the time interval of interest in these experiments, even for the case of sapphire windows (which have a high wavespeed, hence introduce edge effects quickly). Figs. A.7 and A.8 show representative cases.

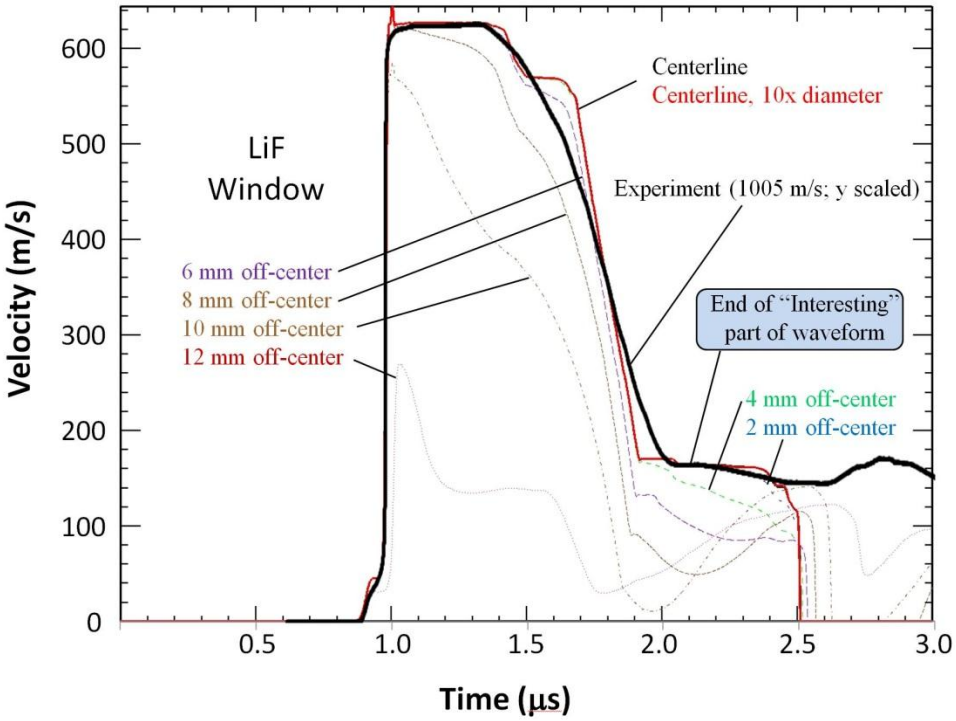

Figure A.7. Results of CTH calculations for a 900 m/s LiF release experiment, with the waveform from the 5 mm sample from SS-2 juxtaposed (vertical amplitude scaled to match 900 m/s impact velocity). The centerline motion follows the zero-edge-effect calculation throughout the time range.

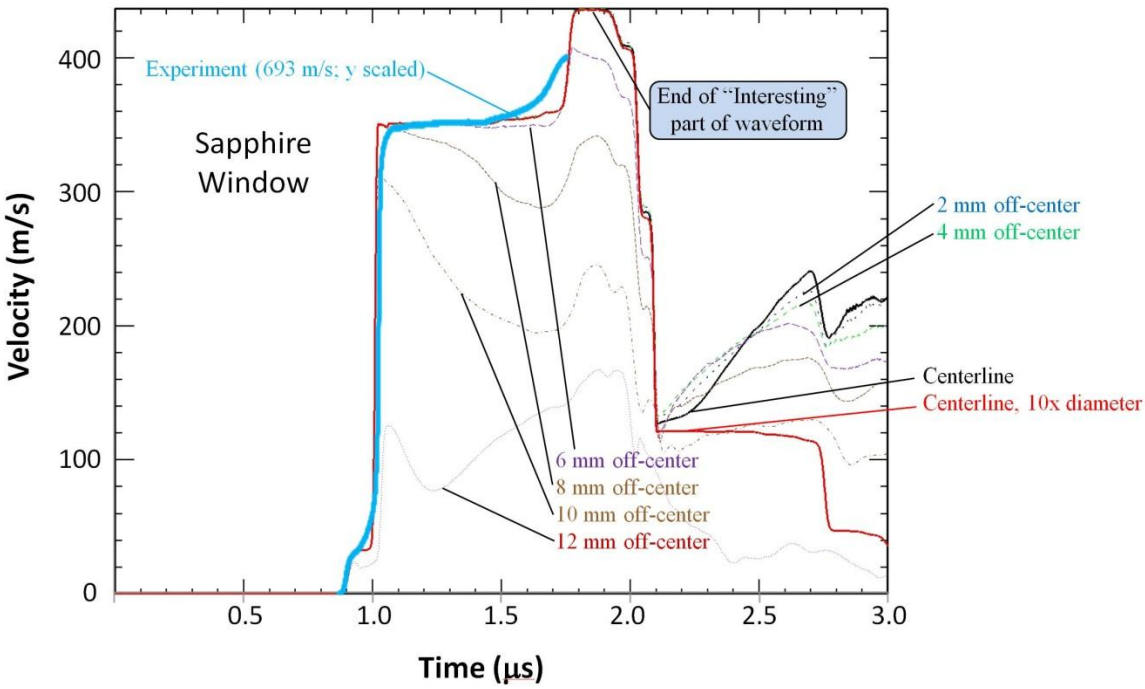

Figure A.8. Results of CTH calculations for 900 m/s sapphire window reshock experiment, with the waveform from the SS-6 reshock sample (vertical ampl. scaled to match 900 m/s impact velocity). The centerline motion follows the zero-edge-effect calculation until after the desired waveform has passed.

Appendix B:
Data and Lagrangian Reduction Plots and Tables Not Presented Earlier

The following plots, not presented elsewhere in this report, are included in this appendix for completeness. These data may also be obtained from the authors as computer files. As well, the complete table of precursor and Hugoniot conditions is included as Table B.1.

Figure B.3 shows the calculation of $\Delta\tau_u$ for experiments SS-1 through SS-5, and is based on Reduce calculations. As discussed in Section 4, the $\Delta\tau_u$ values for experiments SS-2 through SS-5 are probably low by factors approaching 2, and further, any corrected values represent ~80% of the strength. Results from SS-1 (which has a sapphire window, and is less affected by characteristics bending) suggest a strength of 0.9 GPa × 1.25 = 1.12 GPa, which is consistent with the results from the transfer function method shown in Fig. 4.11.

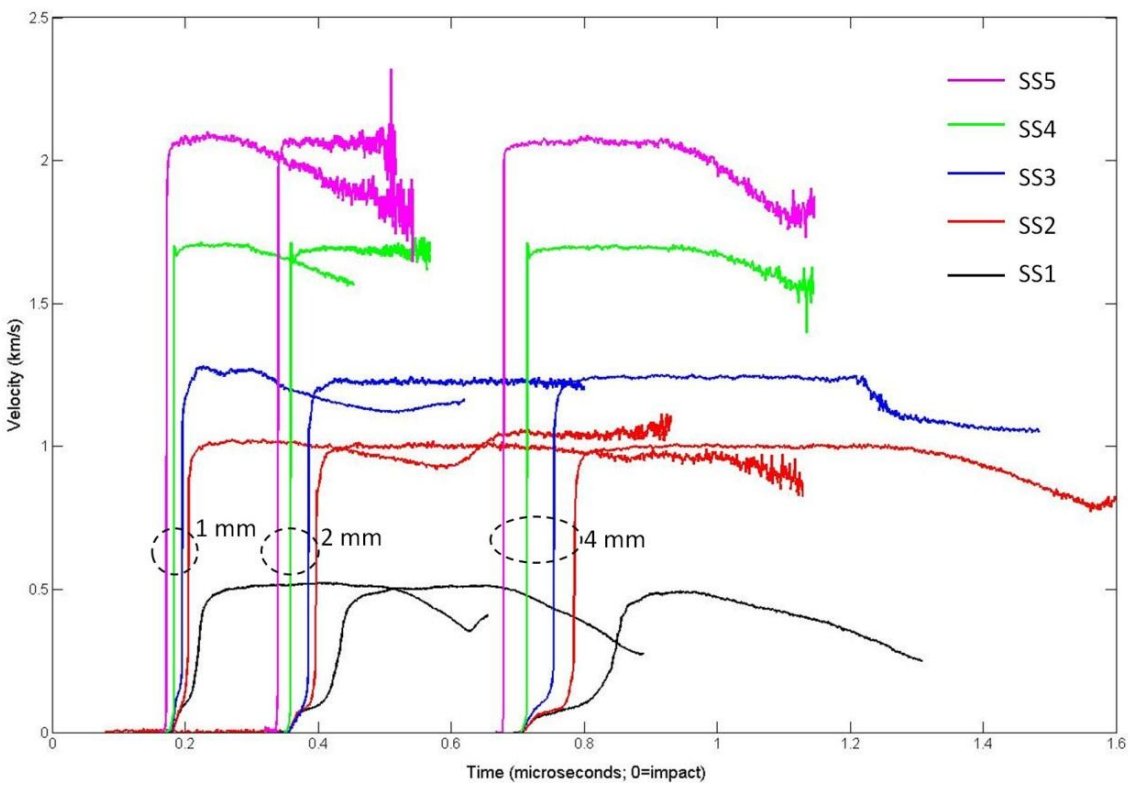

Figure B.1. Velocity histories for free surface (stepped samples) spots on SS-1 through SS-5.

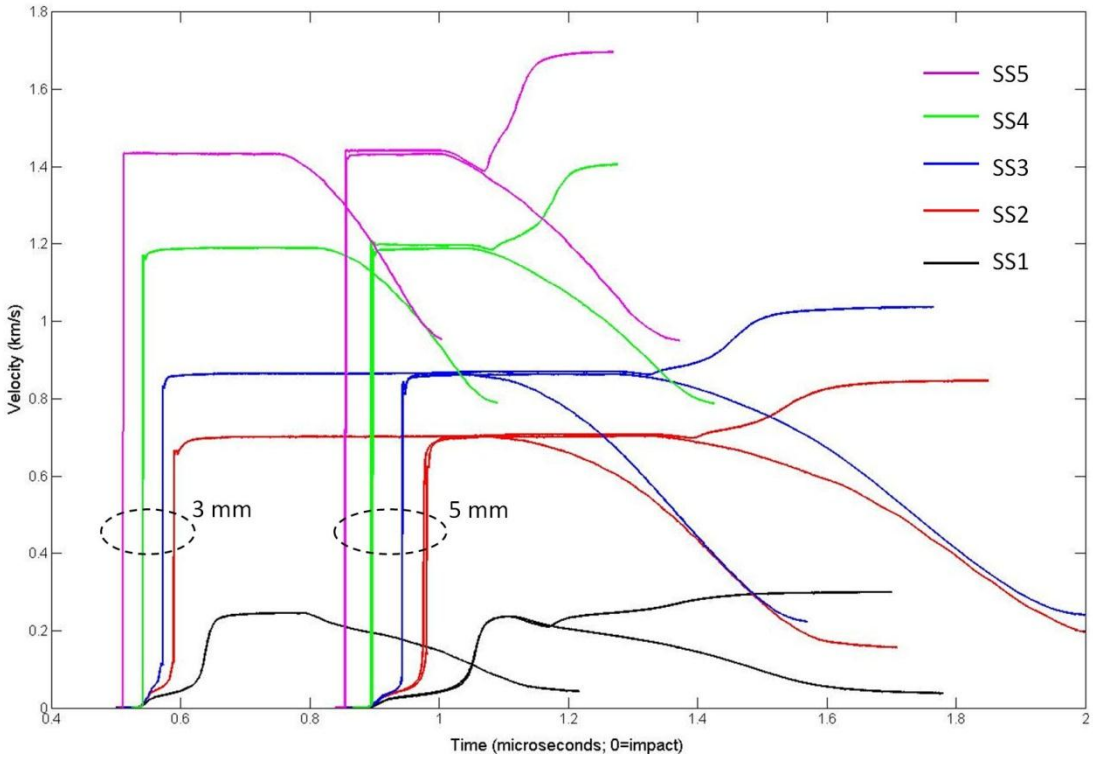

Figure B.2. Velocity histories for windowed spots on SS1 through SS-5.

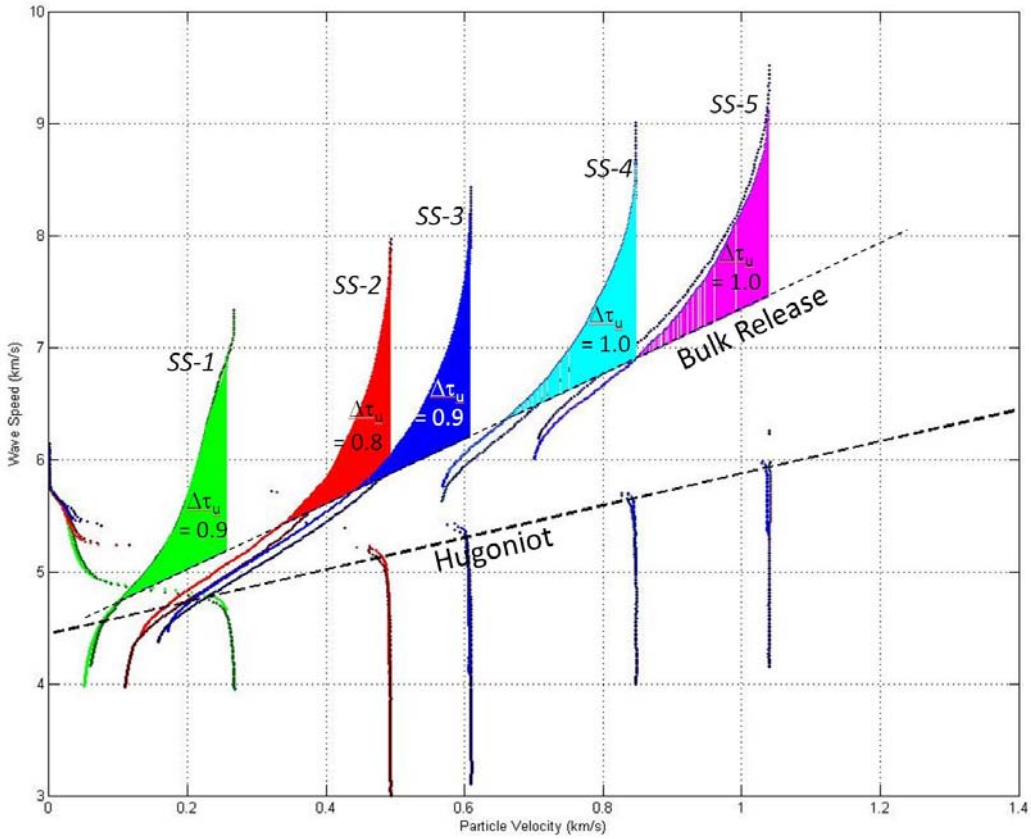

Figure B.3. Integration spaces and values for $\Delta\tau_u$ for shots SS1 - 5 (5 mm samples). Features below the Hugoniot and at the left margin are from the initial loading portion of the analysis.

Table B.1. Detailed Hugoniot and precursor conditions – windowed samples. "NA" means the precursor was mostly or completely overdriven,

		Precursor		Hugoniot				
Shot / Sample	Window	Particle Vel (km/s)	Stress (GPa)	U_S (km/s)	U_P (km/s)	P (GPa)	ρ (gm/cm^3)	Strain
1/1	Sapphire	0.013	0.56	4.833	0.260	9.93	8.27	0.0534
1/2	Sapphire	0.013	0.56	4.853	0.260	9.97	8.27	0.0532
1/3	Sapphire	0.024	1.10	4.834	0.260	10.01	8.27	0.0530
2/1	LiF	0.030	0.95	5.228	0.503	20.28	8.66	0.0956
2/2	LiF	0.030	0.95	5.221	0.503	20.25	8.66	0.0958
2/3	LiF	0.030	0.95	5.237	0.503	20.31	8.66	0.0955
3/1	LiF	0.029	0.91	5.429	0.621	26.08	8.84	0.1142
3/2	LiF	0.029	0.91	5.417	0.621	26.03	8.84	0.1144
3/3	LiF	0.054	1.70	5.389	0.621	25.62	8.84	0.1147
4/1	LiF	NA	NA	5.706	0.856	38.26	9.21	0.1501
4/2	LiF	NA	NA	5.717	0.856	38.33	9.21	0.1498
4/3	LiF	NA	NA	5.712	0.856	38.30	9.21	0.1499
5/1	LiF	NA	NA	5.990	1.032	48.41	9.46	0.1723
5/2	LiF	NA	NA	5.990	1.032	48.41	9.46	0.1723
5/3	LiF	NA	NA	5.990	1.032	48.41	9.46	0.1723
6/1	Sapphire	0.035	1.58	4.950	0.347	13.64	8.41	0.0691
6/2	Sapphire	0.035	1.58	4.950	0.347	13.64	8.41	0.0691
6/3	Sapphire	0.035	1.58	4.909	0.347	13.54	8.42	0.0696
7/1	LiF	0.041	1.29	5.441	0.652	27.31	8.89	0.1195
7/2	LiF	0.041	1.29	5.453	0.652	27.37	8.89	0.1192
7/3	LiF	0.037	1.18	5.411	0.652	27.21	8.90	0.1201
8/1	LiF	NA	NA	5.950	1.005	46.82	9.42	0.1689
8/2	LiF	NA	NA	5.950	1.005	46.82	9.42	0.1689
8/3	LiF	NA	NA	5.950	1.005	46.82	9.42	0.1689

Table B.2. Detailed Hugoniot and precursor conditions – free surface samples. "NA" means the precursor was mostly or completely overdriven.

	Precursor		Hugoniot				
Shot / Sample	Particle Vel (km/s)	Stress (GPa)	U_S (km/s)	U_P (km/s)	P (GPa)	ρ (gm/cm^3)	Strain
1 / 1 mm	0.082	1.85	4.714	0.26	8.4	8.26	0.0522
1 / 2 mm	0.064	1.44	4.749	0.26	8.71	8.26	0.0525
1 / 4 mm	0.045	1.01	4.826	0.26	9.83	8.28	0.0539
2 / 1 mm	0.08	1.8	5.088	0.503	18.6	8.67	0.0971
2 / 2 mm	0.065	1.46	5.157	0.503	19.11	8.66	0.0962
2 / 4 mm	0.06	1.35	5.186	0.503	20.4	8.67	0.0969
3 / 1 mm	0.071	1.6	5.258	0.621	24.23	8.87	0.1171
3 / 2 mm	0.09	2.03	5.309	0.621	24.08	8.86	0.1158
3 / 4 mm	0.11	2.48	5.377	0.621	26.16	8.85	0.1155
4 / 1 mm	NA	NA	5.575	0.856	37.38	9.25	0.1536
4 / 2 mm	NA	NA	5.66	0.856	37.95	9.23	0.1513
4 / 4 mm	NA	NA	5.682	0.856	38.09	9.22	0.1507

(continued on next page)

Table B.2 (continued)

	Precursor		Hugoniot				
Shot / Sample	Particle Vel (km/s)	Stress (GPa)	U_S (km/s)	U_P (km/s)	P (GPa)	ρ (gm/cm^3)	Strain
5 / 1 mm	NA	NA	5.99	1.032	48.41	9.46	0.1723
5 / 2 mm	NA	NA	5.99	1.032	48.41	9.46	0.1723
5 / 4 mm	NA	NA	5.99	1.032	48.41	9.46	0.1723
6 / 1 mm	0.098	2.21	4.757	0.347	11.43	8.41	0.0695
6 / 2 mm	0.085	1.92	4.869	0.347	11.86	8.41	0.0686
6 / 4 mm	0.063	1.42	4.984	0.347	12.47	8.4	0.068
7 / 1 mm	0.092	2.08	5.319	0.652	25.35	8.91	0.1214
7 / 2 mm	0.063	1.42	5.373	0.652	26.18	8.9	0.1206
7 / 4 mm	0.055	1.23	5.446	0.652	26.69	8.89	0.1192
8 / 1 mm	0.048	1.08	5.95	1.005	45.68	9.42	0.1692
8 / 2 mm	0.043	0.97	5.95	1.005	45.8	9.42	0.1691
8 / 4 mm	0.014	0.32	5.95	1.005	46.82	9.42	0.1689

Distribution

Internal:

MS 1189	Dept. 1640	M. Herrmann (electronic copy)
MS 1195	Dept. 1646	D. G. Flicker (electronic copy)
MS 1195	Dept. 1646	C. S. Alexander (5+electronic copy)
MS 1195	Dept. 1646	J. L. Brown (3+electronic copy)
MS 1195	Dept. 1646	J-P. Davis (electronic copy)
MS 1195	Dept. 1646	D. H. Dolan III (electronic copy)
MS 1195	Dept. 1646	M. D. Furnish (5+electronic copy)
MS 1195	Dept. 1646	M. D. Knudson (electronic copy)
MS 1195	Dept. 1646	W. D. Reinhart (3+electronic copy)
MS 1195	Dept. 1646	J. L. Wise (electronic copy)
MS 1195	Dept. 1647	J. R. Asay (electronic copy)
MS 1195	Dept. 1647	R. J. Hickman (electronic copy)
MS 1195	Dept. 1647	G. Leifeste (electronic copy)
MS 1195	Dept. 1647	T. Thornhill (electronic copy)
MS 9046	Dept. 8246	T. Vogler (electronic copy)
MS 0899	Dept. 9536	Technical Library (electronic copy)

External:

Mukul Kumar, LLNL (electronic copy)
Bryan Reed, LLNL (electronic copy)
Jeff Florando, LLNL (electronic copy)
Lalit C. Chhabildas, AFRL (electronic copy)
Rick Martineau, LANL (electronic copy)
Brad Wallin, LLNL (electronic copy)
Robert Hanrahan, NNSA (electronic copy)

Sandia National Laboratories